

EOS/AMSR RAINFALL

Algorithm Theoretical Basis Document

Thomas Wilhelm, Christian Kummerow, Ralph Ferraro

May 1999

1.0 OBJECTIVES

The aim of the precipitation algorithm is threefold: The first is to produce instantaneous rainfall intensity on a pixel-by-pixel basis (Level 2). In addition to rainfall intensity, over ocean, rainfall will be categorized as convective or stratiform. The rainfall, as well as the latent heating which can be derived from the convective/stratiform separation play an important role in Global Circulation Model (GCM) initialization as well as data assimilation efforts currently underway; The second objective is to produce estimates of monthly totals on a $5^{\circ}\times 5^{\circ}$ basis (Level 3). This product is aimed particularly at climate monitoring as well GCM validation. The distinction between instantaneous and monthly products, aside from the applications, is necessitated by the poor temporal sampling of the AMSR instrument. Fortunately, there are statistical properties of rainfall, which can be exploited in order to gain greater confidence in monthly rainfall accumulations. The third objective is to generate credible uncertainty estimates. This requires that the algorithms, to the maximum extent possible, be based on models with well-established physics. The detection of changes on a wide variety of space and time scales is extremely important. By avoiding the use of arbitrary tuning parameters, especially those that vary seasonally and regionally, we have a high degree of confidence that any change we see in the retrieved rainfall is a change in the actual rainfall rather than of some tuning parameter. The physical basis further insures that rainfall estimates made from AMSR can be easily adapted to previous as well as future sensors. In such a way, it will be possible to extend AMSR rainfall climatologies backward to 1987 using SSM/I observations. It will also insure that knowledge gained from the TRMM mission is easily incorporated into the AMSR retrieval. In the ensuing discussion, the reader will see that we have been reasonably, if imperfectly, successful in approaching this goal for the ocean algorithms, where a large and reasonably constant reflectivity of the ocean background enables approaches that are simply not possible if there is a significant amount of land in the field of view. Unfortunately, for the land algorithms, much less has proved possible.

2.0 BACKGROUND INFORMATION

2.1 PHYSICAL BASIS

The application of the theory of radiative transfer to microwave radiances measurable by the AMSR forms the basis of precipitation estimation algorithms. In the theory of radiative transfer (Chandrashekar, 1960), if a radiance, R_i , at a wavelength, λ , is incident on a surface with a reflectivity, r , and a temperature T_s , the radiance of the reflected beam, $R_r(\lambda)$, is given by:

$$R_r(\lambda) = r R_i(\lambda) + \varepsilon B(\lambda, T_s) \quad (1)$$

Where $B(\lambda, T_s)$ is the blackbody radiance (Planck function) for a wavelength, λ , and a temperature T_s . The quantity ε is called the emissivity of the surface. The emissivity, or equivalently the reflectivity (the Second Law of Thermodynamics requires that: $r + \varepsilon = 1$), of the surface is described by the Fresnel relations, (Jackson, 1962), and is determined by the view angle, the polarization and the complex index of refraction of the surface material. It is modified somewhat by roughness of the surface and can also be greatly reduced by vegetation cover. In remote sensing, polarization is termed "horizontal" if the electric field vector of the wave lies in the horizontal plane. The electric field of a vertically polarized wave is perpendicular to both the horizontal polarization and to the direction of propagation. If the view direction is directly at the nadir or the zenith, all polarizations would be horizontal so that this definition becomes useless and the polarization must be defined in some other way. There is generally little or no polarization dependence for nadir viewing in any case.

In Figure 1, typical reflectivities for ocean and land conditions are shown. In both cases the upper curve is for the horizontal polarization and the lower for vertical polarization. The typical land case is computed for complex index of refraction of $2 + 0.1i$, which is reasonable for a moderately dry soil. The ocean case is computed for a complex index of refraction of $6.76 + 2.70i$, which is the value for a frequency of 19.35 GHz and a temperature of 300°K. This large difference in the reflectivities between land and ocean is the reason that the island and continents are so obvious in Figure 2.

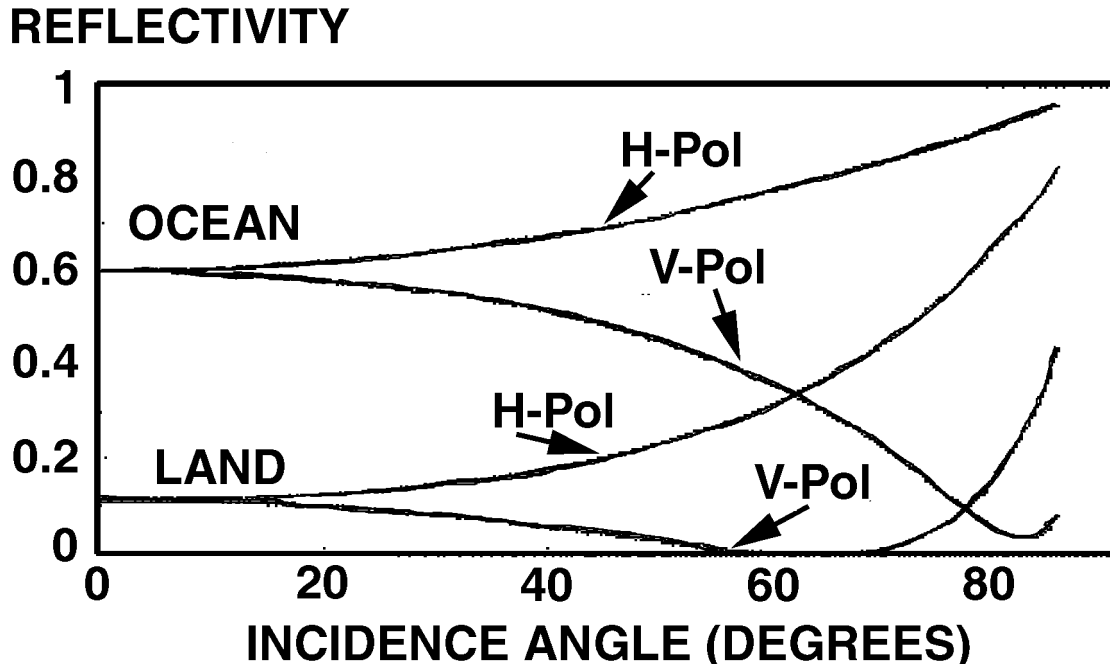


Figure 1: Reflectivity of typical ocean and land surfaces as a function of incidence angle for horizontal and vertical polarizations.

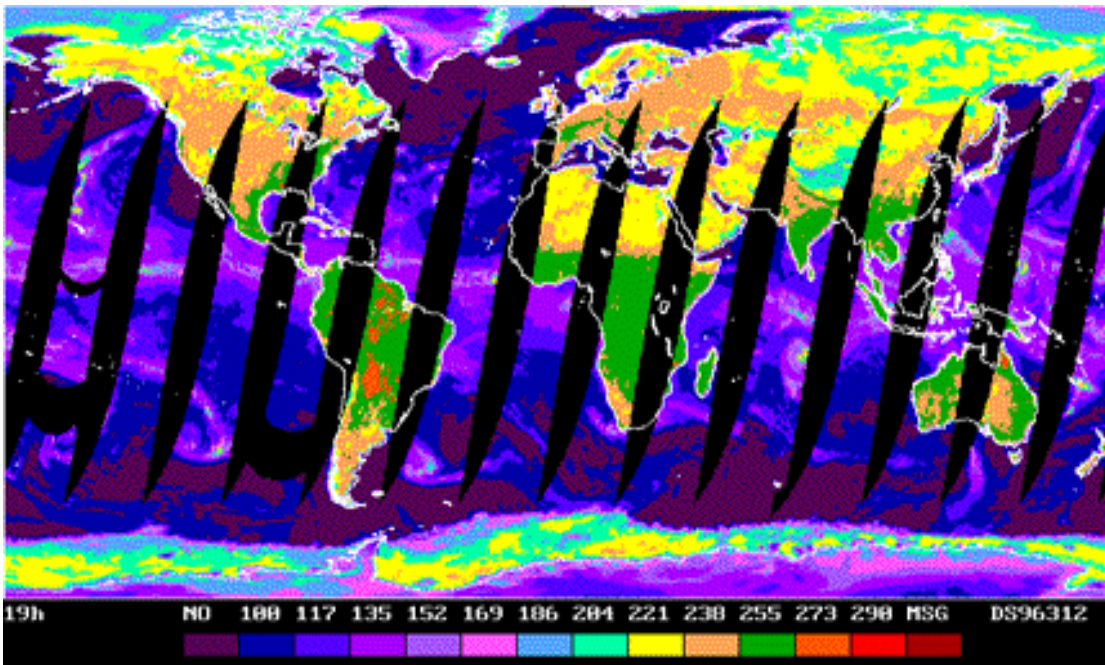


Figure 2: Global brightness temperature composite of SSM/I 19 GHz, horizontal polarization data for descending orbits of F13 satellite on November 7, 1996.

In an atmosphere that absorbs and/or scatters microwave radiation, the radiance is governed by the Equation of Radiative Transfer (RTE) (Chandrashekar, 1960) which may be organized as:

$$\frac{dR(\theta, \phi)}{ds} = A + S \quad (2)$$

where: $A = \gamma_{abs} \{B(\lambda, T) - R(\theta, \phi)\}$ and $S = \gamma_{sca} \left\{ \int P(\theta, \phi; \theta', \phi') R(\theta, \phi') d\Omega' - R(\theta, \phi) \right\}$,

$R(\theta, \phi)$ is the radiance in the direction specified by the polar angles, θ and ϕ , s is distance in the θ, ϕ direction, γ_{abs} is the absorption coefficient and γ_{sca} is the scattering coefficient.

$P(\theta, \phi, \theta', \phi')$, the phase function, describes the probability of scattering from a direction specified by θ', ϕ' to a direction θ, ϕ and is normalized such that:

$$\int P(\theta, \phi; \theta', \phi') d\Omega' = \int P(\theta, \phi; \theta', \phi') d\Omega = 1.$$

With the RTE organized in this manner, the term, A , represents the absorption and concomitant emission and the term, S , represents the loss of radiance due to scattering out of the beam and the gain of radiance due to scattering of radiance traveling in other directions being scattered into the beam with no net change in the total radiation.

The long wavelengths of microwave radiation permit us to make use of the Rayleigh-Jeans approximation, $B(\lambda, T) \propto \lambda^{-4} T$, and to define a brightness temperature, Tb , accordingly.

The RTE can then be somewhat simplified to:

$$\frac{dTb(\theta, \phi)}{ds} = A_{RJ} + S_{RJ} \quad (3)$$

where: $A_{RJ} = \gamma_{abs} \{T - Tb(\theta, \phi)\}$ and $S_{RJ} = \gamma_{sca} \left\{ \int P(\theta, \phi; \theta', \phi') Tb(\theta', \phi') d\Omega - Tb(\theta, \phi) \right\}$.

In the absence of scattering, the RTE could be directly integrated, but, when scattering is introduced to the problem, it becomes significantly more difficult. From examination of the scattering term of eq'ns (2) and (3), one can see that the computation of the radiance at any one angle requires knowledge of the radiance at all other angles. The equations can be set up for a simultaneous solution for all the radiances (the discrete ordinate method) (Goody and Yung, 1989), but if there are very many spatial points to be described and if the

angular distribution of radiances is described with much resolution, the problem quickly gets out of hand and exceeds any given computer capacity. One can also solve the problem iteratively using a first guess or the previous iteration to provide the needed radiances in the scattering term. If scattering is strong, the speed of convergence is very sensitive to the quality of the first guess. In the microwave regime, the radiative transfer problem has a high degree of symmetry. This allows for a number of other methods that are computationally moderate to be used. Examples for plane parallel atmospheres may be found in Wilheit *et al.*, (1977) and Kummerow (1993). The latter shows that errors for these approximations in the microwave regime are typically of the order of only a few degrees Kelvin. Reverse Monte Carlo methods, although computationally more intensive, are also available to treat three-dimensional radiative transfer problems in the microwave spectrum (Roberti *et al.*, 1994).

While the interested reader is referred to the above references for details of the solution to the RTE, it is nonetheless important to develop some insight into the behavior of the solutions. For this purpose, the conceptually simplest solution is the so-called "Reverse Monte-Carlo" solution. Imagine that the radiometer is, for the moment, a transmitter sending photons into the atmosphere for which a computation of the brightness temperature is desired. As each photon propagates through the atmosphere, it has a probability of being absorbed or scattered and, if scattered, a probability distribution of angles. A random number generator is used to determine the fate of the photon in accordance with these probabilities as it proceeds through each incremental distance through the atmosphere. Many photons are sent from the transmitter into the atmosphere and tracked until they are absorbed. The temperature of the atmosphere at the point of absorption is noted and averaged for all the photons. With scattering, there is some probability that the photon will scatter back out of the atmosphere into space. This is equivalent to being absorbed by the 2.7K cosmic background. By a simple generalization of Kirchoff's law, the average temperature at which the photons are absorbed is the brightness temperature that the radiometer would observe.

Three components of the troposphere are important absorbers. Water vapor, liquid water and molecular Oxygen. Frequencies where absorption due to molecular Oxygen is important (roughly 50 to 70 GHz and near 119 GHz) are used for temperature sounding but are not often used for rainfall sensing. For our purposes, the absorption due to molecular Oxygen is a minor correction needed to be quantitatively correct but not necessary for conceptual understanding.

Non-precipitating cloud particles are of the order of 50 μm or less in diameter, much smaller than the wavelength of microwave radiation ($\sim 1\text{ mm}$). As a result, the Rayleigh approximation (Gunn and East, 1954) applies. In this limit the absorption coefficient is proportional to the cube of the diameter and the scattering coefficient is negligible by comparison. Since the absorption coefficient is proportional to the cube of the diameter, it is also proportional to the volume and mass of the drop. Thus, the absorption coefficient of a cloud is simply proportional to the mass density of the water contained in the cloud independent of the details of the size distribution of the droplets as long as all the particles are much smaller than the wavelength.

Rainfall typically has greater liquid water content than non-raining clouds distributed among much larger drops. The larger size of the raindrops increases their absorption per unit mass and also causes enough scattering that it may no longer be ignored. The theory of scattering and absorption by dielectric spheres was first discussed by Mie, (1908), and applied to the context of rain and clouds by Gunn and East (1954). While mathematically involved, these computations are nonetheless well understood. The introduction of ice above the freezing level greatly increases the importance of scattering. Although the scattering cross section of an ice sphere is comparable to that of a liquid sphere of the same size, the absorption cross section essentially vanishes. Thus, in our mental model, if the ice layer above the liquid hydrometeors is thick, a photon will have many opportunities to scatter out of the atmosphere before being absorbed. For wavelengths of a few millimeters or less, scattering by ice particles with densities and sizes characteristic of rain can result in extremely low brightness temperatures. These very low brightness temperatures do not depend on the background and can be used as an indicator of rain over either land or ocean. The land algorithm discussed in the next section attempts to establish and exploit a quantitative relationship between rain rate and brightness in this scattering regime.

A radiative transfer model for a typical rainfall cloud was given by Wilheit *et al.*, (1977). Here, a Marshall Palmer distribution of raindrops is assumed from the surface up to the freezing level (0°C isotherm). The lapse rate is assumed to be 6.5K/km and the relative humidity is assumed to be 80% at the surface and to increase linearly to 100% at the freezing level and remain at 100% above the freezing level. This set of assumptions couples the freezing level, the surface temperature and the precipitable water; selection of any one of them determines the other two for the purposes of the model. In addition to the

M-P distribution of raindrops, a non-precipitating cloud layer containing 0.5 g/m^3 of cloud liquid water is assumed in the 0.5 km just below the freezing level. This cloud assumption is entirely arbitrary. Indeed, the relationship between the suspended cloud liquid water and the precipitating water droplets will change during the life history of a storm.

Figure 3 shows the results of computations based on this model for frequencies of 6.7, 10.65, 19.35, 37 and 89.0 GHz viewing directly at the 54° incidence angle of the AMSR. An ocean background is assumed. The computations were carried out for several different freezing levels as indicated in the figure. While both horizontal and vertical polarizations are computed, only horizontal polarizations are shown in order to keep the figures legible; the vertically polarized brightness temperature is always equal to or greater than the corresponding horizontally polarized brightness for a given freezing level. Note that at all frequencies, the brightness temperature increase towards a maximum and then drop off as rainfall rates increase even further. The key differences between the frequencies is the range of rainfall rates for which the curve increases (emission region) and the range for which the curves are decreasing (scattering region). The 18.7 GHz curve with a 4-km freezing level is used for illustrative purposes. Brightness temperature increases rapidly with rain rate in the 1 to 10 mm/hr range. It reaches a maximum near 265K and then begins to decrease slowly with increasing rain rate. In the increasing part of the curve, the absorption and concomitant emission dominate. As rain rates continue to increase, the atmosphere is nearly opaque so additional absorption can have little effect. The scattering term, however, continues to increase. Referring back to our Monte-Carlo mental model, consider a photon sent into the atmosphere. It is most likely to be absorbed at a temperature of (or slightly higher than) 273K. However it has some probability of being scattered out of the atmosphere back to space, *i.e.* to be absorbed at a temperature of 2.7K. This relatively modest scattering will slightly lower the average temperature at which the photons are absorbed and thus lower the observed brightness temperature.

The curves for different freezing levels in this brightness temperature versus rain rate (T_b - R) relationship are all separate at low rain rates. The most noticeable difference is seen to exist at 18.7 GHz where the T_b vary by almost 50K. Remembering that the freezing level and the water vapor content (precipitable water) are coupled in the model and that the absorption by water vapor is not negligible at 18.7 GHz (3.5 GHz below the water vapor resonance at 22.235 GHz), it immediately becomes clear that this separation is due to the water vapor contribution to the brightness temperatures.

The 89 GHz relations shown in Fig. 3 display the same behavior as the 18.7 GHz. However, because the absorption as well as scattering coefficients are very much larger at 89 GHz, the T_b to rainfall relations reach saturation at very low rainfall rates. For rainfall rates greater than approximately 1 mm/hr, the relationship decreases monotonically. This is the scattering regime referred too earlier.

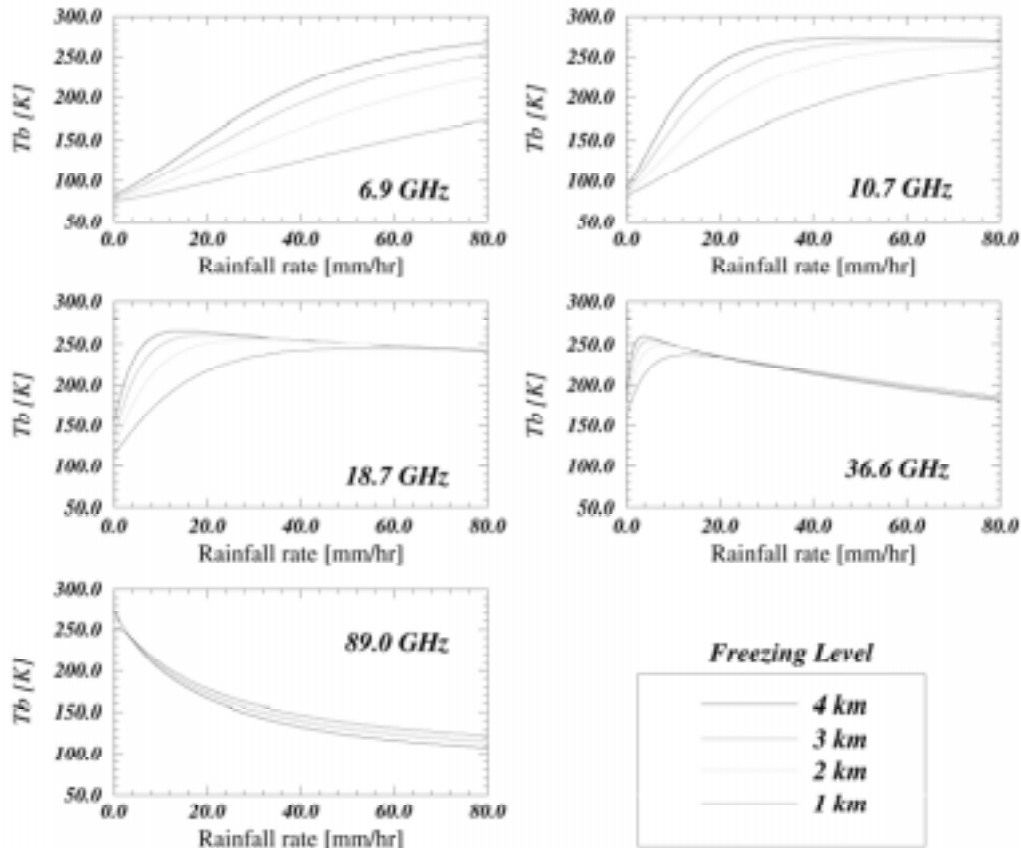


Figure 3: Computed brightness temperatures as a function of rainfall rate for selected AMSR frequencies.

In these computations, the brightness temperature at low frequencies is predominantly a function of the total absorption (in Eq'n 3) with the scattering being a minor correction. This is particularly true in the ascending portion of the T_b - R relationship. Thus, observations in this part of the dynamic range could be considered a measure of the absorption coefficient, γ_{abs} , assuming the thickness of the absorbing layer is known. The

ascending portion of the R-T relationship over ocean is termed the emission (or absorption) regime for rainfall measurements. The rain rate follows from the absorption coefficient implied by the measurements. In contrast, the descending portion of the R-T relations can be considered a measure of the scattering coefficient, γ_{sca} . This regime is generally referred to as the scattering regime. Because frozen hydrometeors are much more efficient scatterers of microwave radiation than their liquid equivalents, the scattering regime is most sensitive to the frozen hydrometeors. Over the high emissivity land background, only scattering signatures present any real information. The rainfall rate over land, therefore, must be inferred from the ice scattering signature instead of relying directly on the emission signal from raindrops.

The absorption coefficient, γ_{abs} , as well as the scattering coefficient, γ_{sca} , can be expressed as an integral over the drop size distribution. If we ignore up- and downdrafts, it is straightforward to express the rain rate itself in this manner.

$$R = \int V(D)(\pi D^3 / 6)N(D)dD \quad (4)$$

where $V(D)$ is the fall speed of the drops as a function of their diameter, D , (Foote and duToit, 1969), $N(D)$ is the number density of drops with diameters between D and $D + dD$; and the volume of a drop of diameter D is $\pi D^3/6$.

In general we can express many parameters in the form: $P_i = F_i \int D^3 N(D) dD$, where F_i is a generic function, the specific form of which depends on the desired parameter P_i . We have chosen to group the D^3 factor with the drop size distribution for graphical clarity; this gives us a volume-weighted drop size distribution. In this form the factor for rain rate F_{RR} is simply $\pi V(D)/6$. The factor for absorption coefficient F_{ABS} is then proportional to the ratio of the Mie absorption to the Rayleigh absorption because of the D^3 factor grouped with $N(D)$.

Because typical ground based radars have frequencies below about 6 GHz, raindrops are well within the Rayleigh regime resulting in a backscatter coefficient proportional to D^6 . Since a factor of D^3 is grouped with $N(D)$, this leaves F_{BS} as proportional to D^3 . In Figure 4, F_{RR} and F_{ABS} for 19.35 GHz are shown. $D^3 N(D)$ is also given for a Marshall-Palmer

distribution at 10 mm/hr. Although the M-P distribution is unique for a given rain rate, actual drop size distributions can vary a great deal for a given rain rate. Note that F_{RR} and F_{ABS} are very similar through the range where $D^3N(D)$ is large. Thus, small changes in N will effect the rain rate and the absorption coefficient almost proportionally. That is, an absorption coefficient measurement is almost equivalent to a rain rate measurement independent of the details of the drop size distribution. By way of contrast, a typical radar backscatter measurement, F_{BS} is very different moment from the rain rate; it is dominated by the very largest drops in the distribution. In this representation, F_{BS} would be a cubic curve. Therefore, radar backscatter measurements for a given rain rate are very sensitive to the details of the drop size distribution that generated the given rain rate. This is one of the primary problems in the use of ground based radar in the measurement of rainfall intensity. On the other hand, if radar is used to provide an attenuation measurement (Atlas and Ulbrich, 1978) it has the same lack of sensitivity to the DSD as does the radiometric measurement.

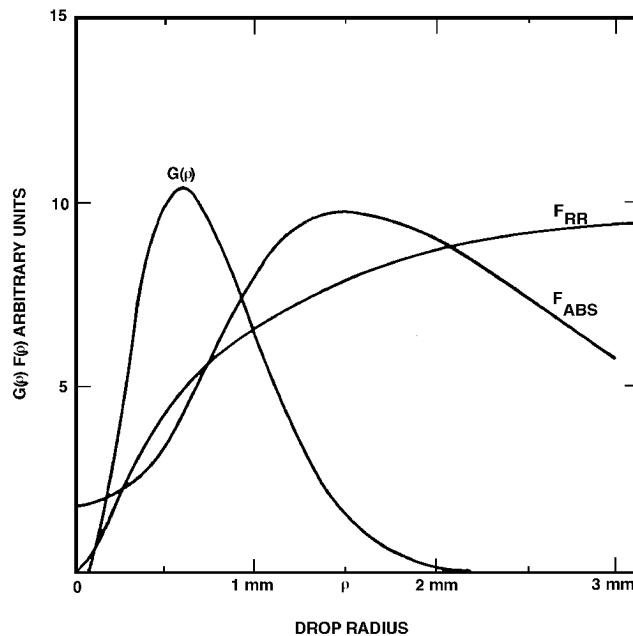


Figure 4: Moments of the drop size distribution (F_{RR} and F_{ABS}) and a volume weighted Marshall Parlmer distribution ($D^3N(D)$), $G(\rho)$, for a 10mm/hr rain rate as a function of the drop diameter.

2.2 HISTORICAL PERSPECTIVE

Characteristic of a number of evolutionary developments in satellite remote sensing of the atmosphere, rainfall estimation proceeded along lines laid out well before the era when the algorithms could achieve full maturity. The early studies took place at the end of the 1960's, a half decade before passive microwave techniques were first examined based on Nimbus 5 Electrically Scanning Microwave Radiometer (ESMR-5) measurements, and initially focused on the idea that a single parameter derived directly from one visible (VIS) or infrared (IR) satellite channel, could be used to estimate a single rainfall parameter related to rain rate or rain accumulation. Such a view prevailed since the VIS and IR channels could only describe the appearance or temperature of the cloud top, and the penetrating spectral channels in the centimeter-millimeter microwave spectrum were not yet available. Thus, rainfall estimation tended to be viewed as a problem in transforming a single input VIS or IR measurement to a single rainfall parameter. Because this VIS-IR heritage, and because the first microwave radiometers were single frequency instruments, the first passive microwave retrieval algorithms continued along the lines of the VIS-IR techniques. For example, the early algorithms proposed by Wilheit *et al.* (1977), Weinman and Guetter (1977), Rodgers *et al.* (1979), and Jung (1980) based on measurements available from the ESMR-5 19 GHz and ESMR-6 37 GHz measurements, were designed to estimate a single rainfall parameter from a single spectral measurement through idealized brightness temperature-rain rate relationships. Once these algorithms achieved certain maturity, however, it was clear that the limited sampling of these polar orbiting platforms would forever be a limiting factor in global rainfall estimates. Much of the attention of the community therefore turned towards the sampling issue with algorithms such as Wilheit *et al.*, 1991 and Berg and Chase, 1992. These studies were supported by growing interests in the statistical nature of the problem (see Bell 1990, North *et al.* 1993)

The first multispectral passive microwave radiometer was the Nimbus 7 Scanning Multichannel Microwave Radiometer (SMMR), was launched in 1987. This instrument created the opportunity for a new class of multichannel algorithms in which different frequencies could detect microphysical activity at different levels within a precipitating cloud, and thus created the possibility for inversion-type schemes designed to retrieve some type of vector describing the rain profile. However, only the study of Olson (1989) over a decade after the launch of SMMR, directly aimed at exploiting the multifrequency SMMR information in a rainfall retrieval algorithm, and then only focusing on hurricane rainfall. A multifrequency study by Kummerow *et al.* (1989) focused on wider applications, but that

study was limited to an examination of aircraft measurements. It was not until the availability of the Special Sensor Microwave Imager (SSM/I) measurements obtained from the Defense Meteorological Satellite Program (DMSP) platforms (see Hollinger *et al.*, 1990), that comprehensive multifrequency precipitation retrieval schemes such as the one being used for AMSR began to evolve; see Smith *et al.* (1994), Mugnai *et al.* (1993), Kummerow and Giglio (1994).

The TRMM mission (launched November 1997) is of particular interest to the AMSR rainfall algorithm because TRMM carries a radiometer (TMI) which has very similar frequencies and resolutions to that of AMSR. Table 1 lists some the relevant TMI parameters, which may be compared to the AMSR instrument characteristics presented in the next section. TRMM also carries a Precipitation Radar which enables us to examine many of the details of the physics of the rainfall measurement.

Table 1. TRMM TMI PERFORMANCE CHARACTERISTICS

Center Frequency (GHz)	10.65	19.35	21.3	37.0	85.5
Bandwidth (MHz)	100	500	200	2000	3000
Sensitivity (K)	0.6	0.5	0.7	0.4	0.9
IFOV (km x km)	63 x 37	30 x 18	23 x 18	16 x 9	7 x 5

Aside from the great similarities between the AMSR and TRMM-TMI instruments, there is also overlap in the rainfall algorithms. In fact, the only difference between the TRMM standard rainfall products from TMI and those for AMSR are adjustments needed to correct for slight frequency and resolution changes. This synergism is possible because two of the AMSR Rainfall ATBD authors (Wilheit and Kummerow) are also key members of the TRMM Passive Microwave team. Thus, information that will be learned from TRMM is immediately available for incorporation into the AMSR rainfall algorithm.

An instrument that needs to be considered from a historical perspective (even though it has not actually been launched yet) is the ADEOS-II AMSR instrument. Since it will be launched approximately one year before the EOS-PM AMSR instrument, these data will afford the group an opportunity to test the algorithm before it becomes operational.

2.3 INSTRUMENT CHARACTERISTICS

The PM-1 AMSR is a twelve channel, six frequency total power passive microwave radiometer system. It measures brightness temperatures at 6.925, 10.65, 18.7, 23.8, 36.5, and 89.0 GHz. Vertically and horizontally polarized measurements are taken at all channels.

The instrument, modified from the design used for the ADEOS-II AMSR, consists of an offset parabolic reflector 1.6 meters in diameter fed by an array of six feedhorns. The reflector and feedhorn arrays are mounted on a drum, which contains the radiometers, digital data subsystem, mechanical scanning subsystem, and power subsystem. The reflector/feed/drum assembly is rotated about the axis of the drum by a coaxially mounted bearing and power transfer assembly. All data, commands, timing and telemetry signals, and power pass through the assembly on slip ring connectors to the rotating assembly.

A cold load reflector and a warm load are mounted on the transfer assembly shaft and do not rotate with the drum assembly. They are positioned off axis such that they pass between the feedhorn array and the parabolic reflector, occulting it once each scan. The cold load reflector reflects cold sky radiation into the feedhorn array thus serving, along with the warm load, as calibration references for the AMSR. Calibration of the radiometers is essential for collection of useful data. Corrections for spillover and other antenna pattern effects are incorporated in the data processing algorithms.

The AMSR rotates continuously about an axis parallel to the local spacecraft vertical at 40 rpm. At an altitude of 705 km, it measures the upwelling scene brightness temperatures over an azimuthal range of +/- 70 degrees about the sub-satellite track, resulting in a swath width of 1500 km.

During a period of 1.5 seconds the spacecraft sub-satellite point travels 10 km. Even though the instantaneous field-of-view for each channel is different, active scene measurements are recorded at equal intervals of 10 km (5 km for the 89 GHz channels) along the scan. The half cone angle at which the reflector is fixed is 46.6 degrees which results in an Earth incidence angle of 53.8 degrees. Table 2 lists the pertinent performance characteristics.

Table 2. PM-1 AMSR PERFORMANCE CHARACTERISTICS

Center Frequency (GHz)	6.925	10.65	18.7	23.8	36.5	89.0
Bandwidth (MHz)	350	100	200	400	1000	3000
Sensitivity (K)	0.3	0.6	0.6	0.6	0.6	1.1
IFOV (km x km)	76 x 44	49 x 28	28 x 16	31 x 18	14 x 8	6 x 4
Sampling Rate (km x km)	10 x 10	5 x 5				
Integration Time (msec)	2.6	2.6	2.6	2.6	2.6	1.3
Main Beam Efficiency (%)	95.3	95.0	96.3	96.4	95.3	96.0
Beamwidth (degrees)	2.2	1.4	0.8	0.9	0.40	0.18

The electromagnetic field throughout this discussion has been characterized as a radiance (or brightness temperature). It must be understood that a radiance is merely a mathematical construct. It is defined over an infinitesimal spectral bandwidth and an infinitesimal solid angle. AMSR measurements, as are all real measurements, are over finite bandwidths and solid angles. Generally in the microwave portion of the spectrum, the finite bandwidth considerations are of little practical importance except to the instrument designer. However, since the microwave wavelengths are comparable to the dimensions of the antenna, diffraction of the radiation severely limits the spatial resolution.

The energy transmitted or received by a microwave antenna is distributed according to a gain function $G(\theta, \phi)$ which is normalized such that: $\int G(\theta, \phi) d\Omega = 4\pi$. For typical remote sensing antennas such as AMSR, the gain function is large through a limited region (the main beam) and then decreases to less than about 1% of its maximum value for all other angles (sidelobes). The full width at half maximum of the main beam is roughly $1.4 \lambda/D$ due to diffraction effects and typically about 90% of the energy is received from angles within about $3\lambda/D$ of the center of the main beam. This gain function is smoothed further by the motion of the antenna during the integration period for each observation. Thus, a radiometer connected to an antenna doesn't measure a brightness temperature but rather an integral over the brightness temperature, which is defined as the antenna temperature:

$$T_a = 1/(4\pi) \int G'(\theta, \phi) T_b(\theta, \phi) d\Omega \quad (5)$$

where the prime on the antenna gain function indicates that the antenna motion during the integration period has been taken into account.

The antenna temperature has contributions from all angles, including those missing the earth and viewing the 2.7K cosmic background directly. Corrections can be made for some of the extraneous contributions. Nevertheless, any measured quantity with any corrections applied still represents a finite range of angles and thereby is not, strictly speaking, a brightness temperature.

The AMSR data as processed contain a correction for the fraction of the antenna gain function that views space directly and for some of the sidelobes near the main beam. We will refer to any radiance estimate derived from AMSR as a "brightness temperature", with the full knowledge that no measured quantity is truly a brightness temperature. Since corrections have been applied, neither is the value an "antenna temperature" and we do not wish to coin additional phrases.

3.0 ALGORITHM DESCRIPTION

3.1 THEORETICAL DESCRIPTION

3.1.1 Instantaneous Ocean Rainfall

Radiative transfer calculations can be used to determine a brightness temperature, Tb , given a temperature, water vapor and hydrometeor profile. An example of such a computation through the cloud structure assumed by Wilheit *et al.*, (1977), was shown in Fig. 3. An inversion procedure, however, is needed to find a rainfall rate, R , given a brightness temperature Tb . At first glance, one might be tempted to simply invert the curves shown in Fig. 3, particularly since the double valued nature of the relations is easily resolved by a combination of two or more channels. It must be recalled however, that the relations derived in that example were applicable only to the 'average' cloud structure assumed in that study. Since Tb are sensitive to the vertical structure of precipitation, the vertical structure cannot be ignored when instantaneous retrievals (Level 2 products) are sought. The sensitivity to the assumed profile gets larger as the frequency increases and the scattering in the upper layers of the cloud begin to play a larger role. Thus, one is left with a somewhat more complicated problem of finding the hydrometeor profile, \mathbf{R} , given a set of Tb represented by the vector \mathbf{Tb} . The objective of the instantaneous rainfall algorithm over ocean is to find this profile \mathbf{R} .

While the vertical structure of precipitation is extremely important in determining upwelling microwave radiances, it cannot, unfortunately, be easily characterized in terms of a single unknown variable. Predefined cloud structures, however, may be utilized to overcome this problem. Cloud resolving models such as the Goddard Cumulus Ensemble model (GCE), which is a cloud microphysical model developed mainly by Tao and Simpson, (1993), or the Tripoli, (1992), model are used to supply the required cloud structures. For each cloud model time step, radiative transfer computations are performed at high resolution. This brightness temperature field is then convolved with the approximate AMSR antenna gain function to produce a large set of possible cloud profiles along with their respective passive microwave brightness temperatures. The main advantage of convolving the high-resolution brightness temperatures is that rainfalls in homogeneities are naturally represented in the method. Having statistically verified the cloud model in homogeneity against ground based radar results; there is thus no further need to make corrections for inhomogeneous rainfall.

Databases are generated separately for different freezing heights to capture the different dynamics of tropical and extratropical rainfall systems. The freezing height is determined using the 19 and 21 GHz channels. Details of the procedure are provided in section 3.1.3. (For the simple reason that the technique was first developed for the monthly rainfall algorithm discussed later).

Once a database of profiles and associated brightness temperatures is established, the retrieval employs a straightforward Bayesian inversion methodology. In this approach, the probability of a particular profile \mathbf{R} , given \mathbf{Tb} can be written as:

$$\Pr(\mathbf{R} | \mathbf{Tb}) = \Pr(\mathbf{R}) \times \Pr(\mathbf{Tb} | \mathbf{R}) \quad (6)$$

where $\Pr(\mathbf{R})$ is the probability that a certain profile \mathbf{R} will be observed and $\Pr(\mathbf{Tb} | \mathbf{R})$ is the probability of observing the brightness temperature vector, \mathbf{Tb} , given a particular rain profile \mathbf{R} . The first term on the right hand side of Eq'n (6) is derived using the GCE model information. The second term on the right hand side of Eq'n (6), is obtained from radiative transfer computations through the cloud model profiles.

The formal solution to the above problem is presented in detail in Kummerow *et al.*, (1996). In summary, the retrieval procedure can be said to compose a new hydrometeor profile by taking the weighted sum of structures in the cloud structure database that are

radiometrically consistent with the observations. The weighting of each model profile in the compositing procedure is an exponential factor containing the mean square difference of the sensor observed brightness temperatures and a corresponding set of brightness temperatures obtained from radiative transfer calculations through the cloudy atmosphere represented by the model profile. In the Bayesian formulation, the retrieval solution is given by:

$$\hat{E}(R) = \sum_j R_j \frac{\exp\{-0.5(Tb_o - Tb_s(R_j))^T (O + S)^{-1} (Tb_o - Tb_s(R_j))\}}{\hat{A}} \quad (7)$$

Here, R_j is a vector of model profile values from the GCE model, Tb_o is the set of AMSR observed brightness temperatures, $Tb_s(x_j)$ is the corresponding set of brightness temperatures computed from the model profile R_j . The variables O and S are the observational and model error covariance matrices, respectively, and \hat{A} is a normalization factor. The profile retrieval method is an integral version of the well-known minimum variance solution for obtaining an optimal estimate of geophysical parameters from available information (ref. Lorenc, 1986, for a general discussion).

The integral form has a number of advantages with respect to earlier iterative forms. In particular, the integral form used by Goddard Profiling algorithm (GPROF) is computationally efficient, since it only requires the evaluation of the weighted average of candidate profiles from the cloud model database. The absence of iterative steps requiring radiative transfer computations inside the retrieval loop further allows the current algorithm to take advantage of improvements in radiative transfer methods. In constructing the GPROF databases, for instance, it is possible to take advantage of newly developed 3-dimensional radiative transfer methods instead of traditional 1-D models. Finally, this form of the solution guarantees that the candidate cloud water/precipitation profiles and heating/moistening profiles in the retrieval procedure are completely consistent with the dynamics and physical processes embodied in the dynamical cloud model.

An example of the profiling capability of GPROF using aircraft radiometers (high spatial resolutions) over water is presented in Figure 5. The top panels show the ER2 Doppler Radar (EDOP) observed reflectivities for the two situations. AMPR observed brightness temperatures are shown in the middle panels. The bottom panels show the reflectivity as derived from the GPROF retrieval. The reflectivity is obtained by converting the retrieved hydrometeor field to an equivalent radar reflectivity. This was done in order to compare

results directly with the reflectivities measured by the EDOP radar flying on the same aircraft and shown in the top panel.

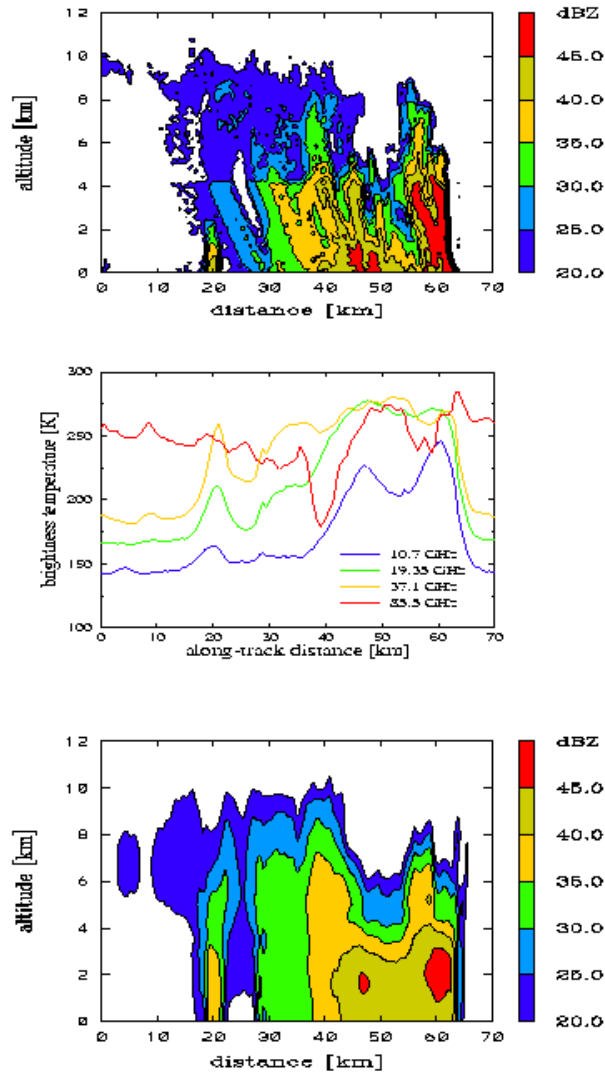


Figure 5: Top panels: EDOP measured reflectivity structure. Center panel: AMPR observed brightness temperatures, at nadir, coincident with EDOP measurements. Bottom panel: Retrieved radar reflectivity from GPROF algorithm. Reflectivities are determined from the cloud model prescribed drop-size distributions. Background is water.

The retrieval is seen to capture the overall structure of the precipitation quite well. Convective, stratiform, and even anvil regions are clearly evident in the GPROF retrievals. Given high spatial resolution, it is clear that there is sufficient vertical structure information in the brightness temperature signal to make profiling retrievals worthwhile. As resolution decreases, however, so does the unique radiometric signature in the satellite *FOV*. Retrievals reflect this loss of unique information by retrieving ever more self-similar profiles. Instantaneous comparisons of rainfall algorithms at the relatively poor resolution of the currently available SSM/I sensors indicate that only modest improvements can be made by retrieving the entire hydrometeor profile when compared to simpler rainfall schemes. Based upon simulated retrievals, the higher resolution of the AMSR will provide significantly greater radiometric signatures that should favor the more physical schemes such as the one described here. Early results from TRMM confirm these simulations.

The loss of radiometric information with sensor resolution forces the retrievals to depend more heavily upon the mean profiles available from the retrieval databases. To test the potential sensitivity of AMSR, we use SSM/I whose significantly lower spatial resolution should provide a limiting case. An example of satellite (SSM/I) derived rainfall is shown in Figure 6. Here, the sensitivity of GPROF to distinct cloud model databases is examined. Panel A shows the tropical oceanic rain system retrieved when a CCOPE simulation is used exclusively for the database. CCOPE is an early spring time continental simulation and should therefore show little similarity to the tropical pacific. Indeed, it is apparent that in the CCOPE retrieval, the core region of the precipitation is missing. Using this database, GPROF found no suitable structures from which to construct a rain profile. The rain field in this case is flagged as “not retrievable”. The remaining three panels consist of a COHMEX, GCE (consisting of a TOGA as well as a GATE simulation), and a HYBRID database which includes all of the above. Qualitatively, the final three outputs appear very similar. Quantitatively, they all agree to within 10% of the total rainfall in the scene. Thus, GPROF is seen not to be overly sensitive to input databases as long as structures that reasonably resemble the observed conditions exist in the database. AMSR retrievals, with better spatial resolution than SSM/I should show even less sensitivity to the input databases.

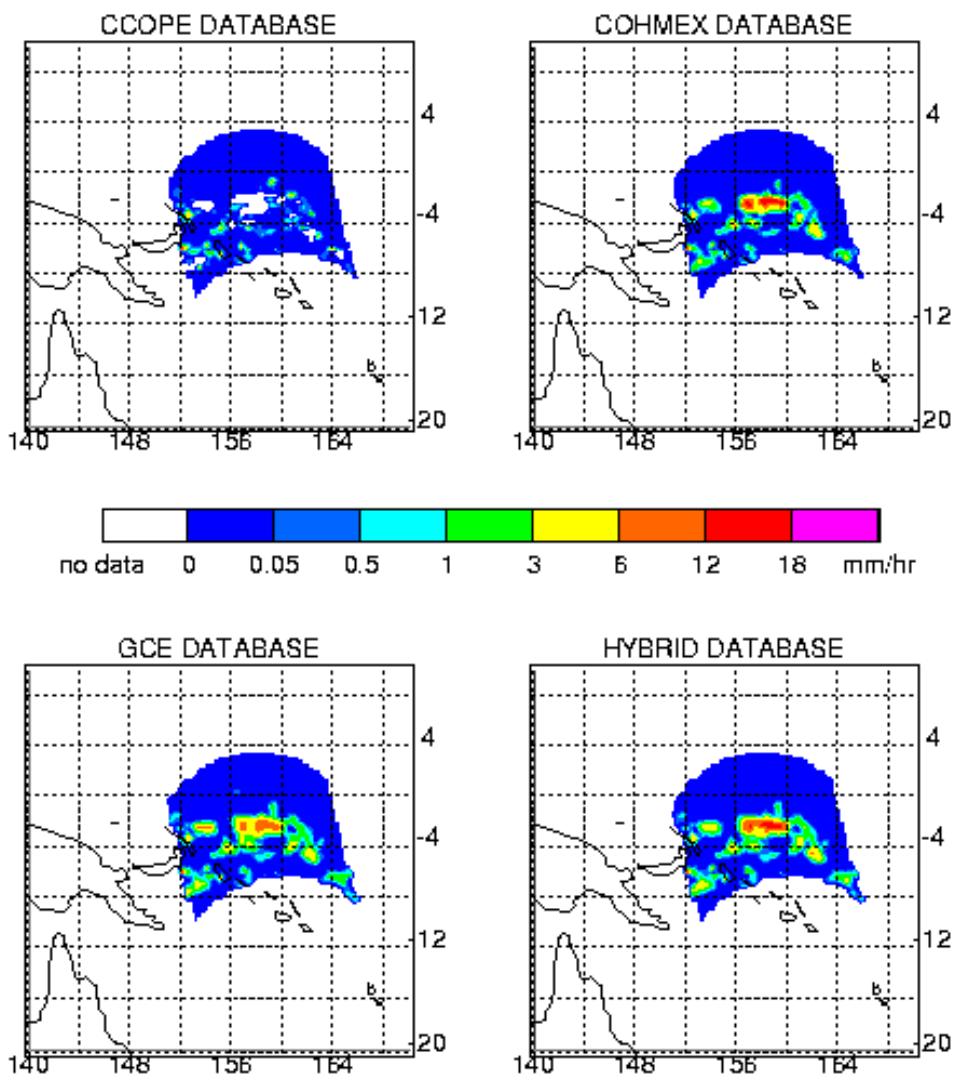


Figure 6: SSM/I retrievals of tropical oceanic rainfall using specified cloud models for retrieval basis. CCOPE model is for continental springtime conditions while the remaining simulations are for tropical environments. The 'missing' areas of rainfall in the CCOPE panel are due to the fact that GPROF could not find suitable cloud structures.

The most important parameter that is needed for global climate studies over oceans is not the rainfall itself, but rather the latent heating released by the rainfall. Tao *et al.* (1990, 1993) have developed algorithms for estimating the latent heating of cloud systems based upon remotely sensed precipitation distributions and vertical hydrometeor structures.

Specifically, two alternative schemes for calculating the latent heating profiles were presented. The first scheme utilized high-resolution vertical precipitating hydrometeor information to infer the latent heating profile. The second scheme utilizes only information regarding the convective or stratiform nature of the precipitation. While the first scheme clearly offers greater accuracy, it is at this time, not yet clear that sufficient information can reliably be supplied for this scheme from the radiometer alone.

The AMSR precipitation team made a decision that a reasonably conservative approach should be used for the operational rainfall algorithm. The decision was therefore made to limit the information regarding the vertical structure to a separation of rainfall into convective and stratiform components. Implementing this approach requires two separate components. The first is to make an a-priori assessment of the convective/stratiform nature of the rainfall. Anagnostou and Kummerow (1997) developed such a scheme based upon the spatial inhomogeneity of the 85 GHz T_b from SSM/I. This scheme was later improved by Hong et al. (1999), to incorporate emission characteristics of the 37 GHz channel. This improvement dealt primarily with the possibility of tilted convection and the need to account for the spatial offset between the 85 GHz scattering signal and the convective elements in a cloud.

The convective/stratiform separation discussed above does not lead to a definitive classification. Instead, it gives the probability of convection based upon the magnitude and nature of the spatial signature. The second step in the convective/stratiform separation follows the same Bayesian approach as discussed above. To implement this option, the Convective/ Stratiform separation (as determined from the cloud dynamical model) is stored in the databases along with the brightness temperatures. The retrieval then follows the same logic discussed earlier, but both the Conv/Strat classification as well as the T_b are used to select the appropriate profiles from the database. This approach, retrieves not only the Conv/Strat nature of the precipitation, but has significantly improved the precipitation retrievals as well.

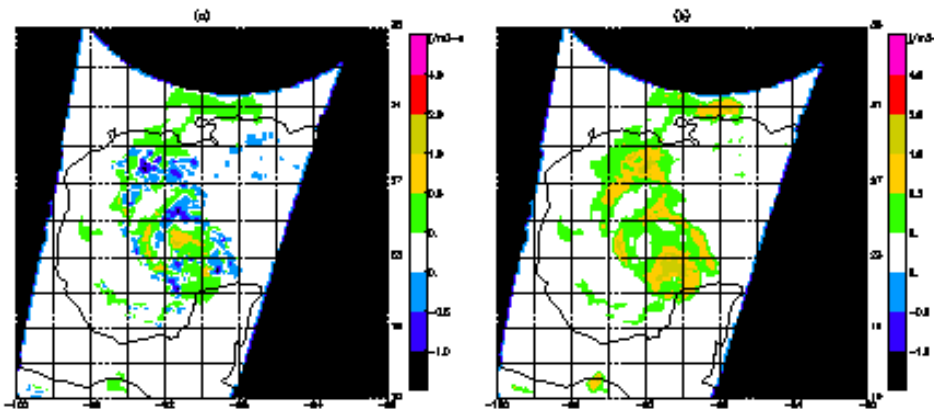


Figure 7: Latent heating for hurricane Opal (1995).

An illustration of what can be accomplished, even with SSM/I resolution, is presented in Figure 7 which shows the latent heating reconstructed from GPROF retrievals for hurricane Opal in 1995. Note the presence of low-level heating in the convective core region of the storm, as well as in the outer convective bands. Low-level cooling between the convective regions indicates the presence of stratiform precipitation. Aloft, heating predominates in both convective and stratiform regions. These distributions are generally consistent with aircraft observations of hydrometeor distributions and vertical motions in tropical cyclones (e.g. Houze *et al.*, 1992).

Most of the GPROF database and algorithm development has been concentrated in the tropics in connection with TRMM. The databases, in particular, are heavily weighted towards the tropics. The physical validation plan described in section 3.2.2 is intended to improve our characterization of extratropical rainfall systems.

3.1.2 Instantaneous Land Rainfall

3.1.2.1 Introduction

Rainfall retrievals over land, as discussed in section 2, are far more difficult than oceanic retrievals due to the large and variable emissivity of the land surface. Specifically, the high emissivity masks the emission signature that is related directly to the water content in the atmosphere. Instead, only the brightness temperature depression due to scattering in the upper portion of clouds is observed. The scattering, as shown in Figure 3, increases with increasing frequencies. Consequently, brightness temperature depressions at the 89 GHz channel of AMSR will contain the least ambiguous signal of scattering by ice and/or large raindrops. The brightness temperature depression will be converted to an expected rainfall rate through the GPROF retrieval scheme where databases of hydrometeor profiles (associated with a variety of rain systems) will be developed for different climatological zones. Recent results from TRMM indicate that the relationship of lightning flashes (which is highly correlated with the 85 GHz scattering signature) and rainfall varies over the global land regions

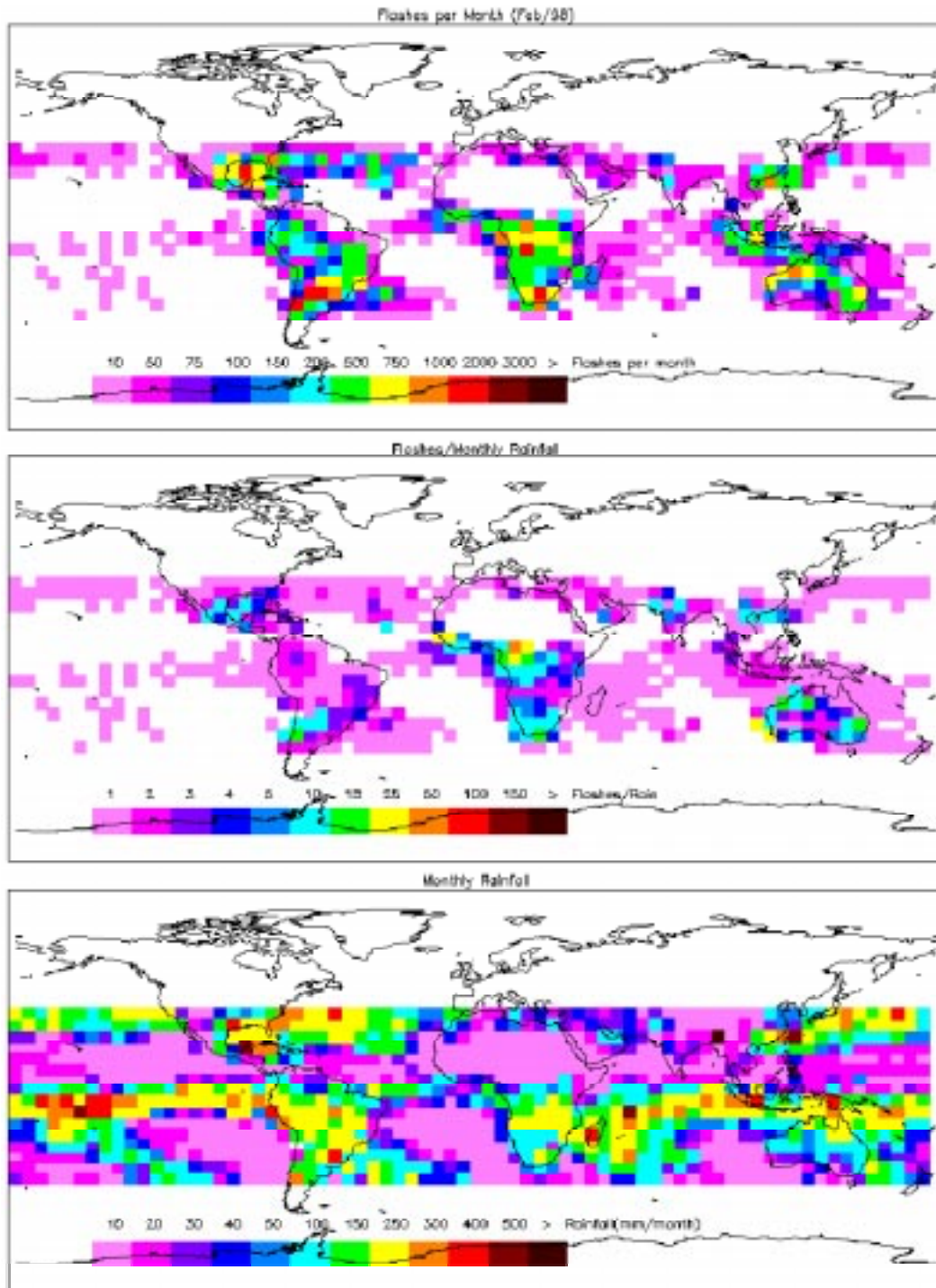


Figure 8: Relationships between lightning and rainfall derived by TRMM. Top panel: number of lightning strikes per 5° x 5° grid box for February 1998. Middle panel: ratio of lightning to rainfall. Bottom panel: Total rainfall derived for the TRMM radar for February 1998.

For example, note how the monthly rainfall in tropical South America and Africa are fairly similar, yet, the amount of lightning in Africa is much larger. In this instance, the globally applied relationship between scattering and rainfall is likely erroneous in Africa (note the study by McCollum, *et al.*, 1999a). Development of profile databases for different climatological zones can account for these differences. However, as a starting point, we will insure that these retrievals match closely with established algorithms developed for the SSM/I and TMI sensors at the time of EOS-PM launch. Details on this procedure follow.

A further complication that arises over land is the lack of consistent backgrounds against which to compare the Tb depression. To alleviate this problem caused by the varying emissivity associated with changes in surface characteristics (e.g., surface wetness, snow cover, vegetation, etc.), a rain/no-rain temperature depression threshold is required. Additionally, snow and desert surfaces cause depressed Tb 's at high frequencies (due to surface volume scattering) and can be confused with the rain signature. If these surface types are not properly screened, they can be misinterpreted as ice scattering in clouds.

3.1.2.2 *Instantaneous Land Rainfall – Rain/No Rain determination*

The “screening” issue has always been one of modest controversy in the land-based retrievals because of the empirical nature of their form. Intuitively, one immediately thinks that such screens will vary greatly with sensor. However, as is described later, these screens (i.e., Tb relationships separating rainfall from other surfaces) seem to hold valid for other sensors, with only minor modifications needed. Additionally, one school of thought in physical retrievals is that the rain rate retrieval becomes a two-step process: rain identification and rain rate determination. This philosophy has been adopted by GPROF and is being utilized for the AMSR retrieval algorithm.

The basis for the retrieval over land comes from the work of Grody (1991), who developed a global scattering index (SI) at 85 GHz for use with the SSM/I sensor. Further refinement of the technique is described in Ferraro *et al.* (1994) and Ferraro *et al.* (1998). The rationale was to first develop a relationship which could best predict the 85 GHz Tb under "non-scattering" conditions for the land surface in question. Then, by estimating this value and subtracting the actual 85 GHz Tb , a measure of the depression due to scattering by precipitation ice/rain drops could be determined. The form of the SI is as follows:

$$SI_{85V} = a + b \cdot Tb_{19V} + c \cdot Tb_{22V} + d \cdot Tb_{22V}^2 - Tb_{85V} \quad (8)$$

where the coefficients a, b, c , and d were derived by assembling a global data set of SSM/I observations under scatter-free conditions. Through an exhaustive evaluation, Grody (1991) found that an SI value of 10 K or greater was a good, global indicator of rain. A lower threshold does detect more rain; however, it also causes the detection of false alarms to increase. Because snow and deserts can cause a similar scattering signature, a set of "screens" were developed to remove such features. The desert check involves the use of polarization information at 19 GHz, while the separation of rain from snow utilizes two relationships involving the Tb at 22 and 85 GHz.

Ferraro *et al.*, (1994), built upon the Grody (1991) study, and developed a more robust set of relationships to be used for the detection of rain over land from the SSM/I. In this study, separate relationships were developed for land and ocean, improving the sensitivity to scattering. In addition, the original relationships derived by Grody (1991) used antenna temperatures which were convolved to the 19 GHz FOV ; the updated study used the more conventional Tb values and preserved the original SSM/I footprint sizes, allowing for easy implementation by the scientific community.

Specifically, the land portion of the algorithm is:

$$SIL - 451.9 - 0.44 \cdot Tb_{19V} - 1.775 \cdot Tb_{22V} + 0.00575 \cdot Tb_{22V}^2 - Tb_{85V} \quad (9)$$

This study also re-derived the relationships to separate rain from snow and deserts and introduced a new screen for semi-arid regions (i.e., the Sahel region of Africa). In summary, the SI values greater than 10K identify rain areas, and subsequent screens remove snow covered, desert, and semi-arid land regions.

McCollum *et al.* (1999b) used SSM/I data to optimize two screening methodologies described in Ferraro *et al.* (1998) and to evaluate both methods to document and improve their deficiencies. The two methodologies are the NESDIS screening of Ferraro (1997) and the GSCAT2 screening used in GPROF 4.0 algorithm, and at this writing, in TRMM TMI production algorithm. In general, the NESDIS based screening tends to be more liberal in nature and allows for rain identification in colder environments (at the expense of misclassification due to melting snow) while GPROF is more conservative, and flags these areas as indeterminate (at the expense of eliminating moderate to heavy rainfall in winter seasons). GPROF also appears to suffer from some inadequate screening in semi-arid

areas. McCollum *et al.* (1999b) developed a methodology that adopts the more conservative GPROF approach but uses spatial information from neighboring pixels to “fill-in” indeterminate areas. An additional modification to previous rain/no-rain temperature depression thresholds was made. To depart from the scattering index (Eq. 8) threshold, which was determined specifically for SSM/I data, a more generic difference between low and high frequency SSM/I channels is used. A 22V - 85V threshold of 8K was found to be appropriate for identification of pixels with rain.

Shown in Figure 9 is an example of rainfall rates from the NESDIS, GPROF, and screens for an SSM/I overpass January 2, 1999. This figure illustrates the benefit of the new screen. The snow line was near the Indiana/Kentucky border that day, so ideally there would be estimates south of the snow line and no estimates (indeterminate) north of this line. The original screens classify all but the southernmost areas of the rainfall as indeterminate, while the new screen captures the true rainfall up until just south of the true snow line.

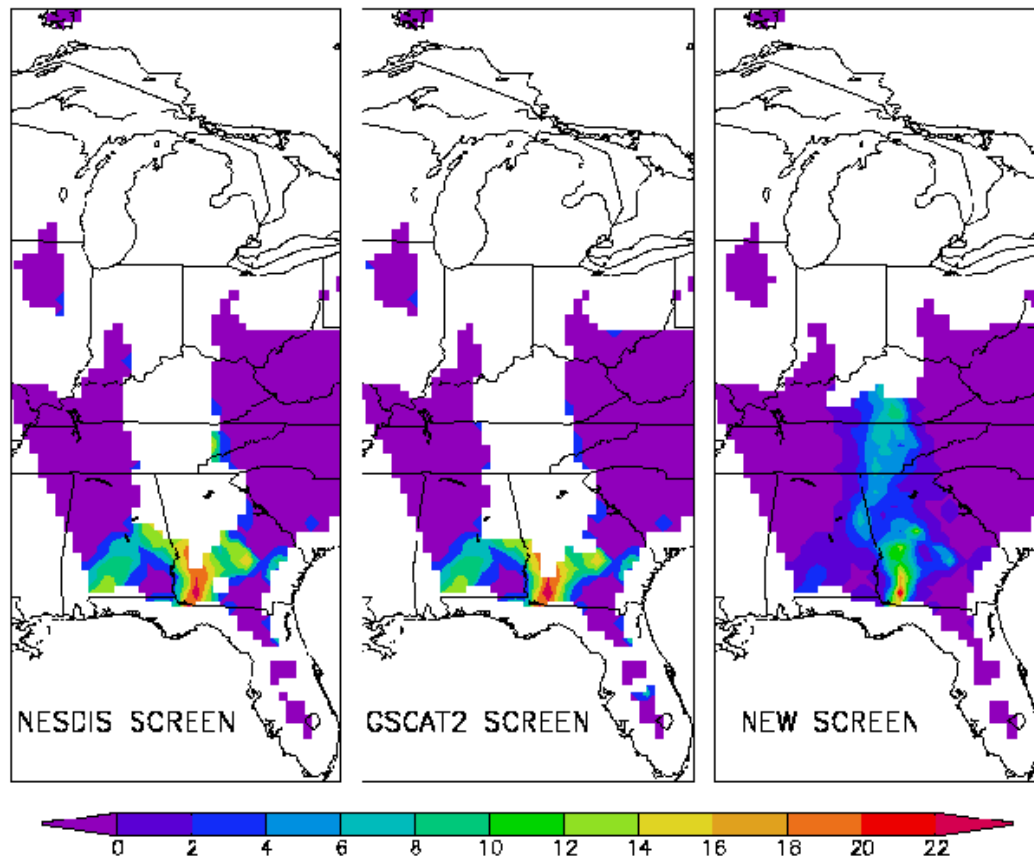


Figure 9. Comparison of rainfall rates (mm/h) from GPROF with different screens for an SSM/I overpass on January 2, 1999. Rainfall rates are in mm/h.

Although we previously thought that screening procedures cannot easily be modified from SSM/I to other sensors because they are empirically derived, recent experience with the NOAA-15 AMSU has proven otherwise. Although resolution and frequency changes do impact these screens, we now feel that these will be minor in nature. Shown in Figure 10 are some global daily composites of SSM/I F13 (top), AMSU (middle) and SSM/I F14 for April 29, 1999. The screening logic for AMSU was based on those described by Ferraro *et al.* (1998) and required very little change, despite the large difference in the AMSU sensor from SSM/I. One residual problem noted in AMSU is deserts (e.g., see the Sahara and Australian deserts), and this is due to the lack of polarization on the AMSU instrument.

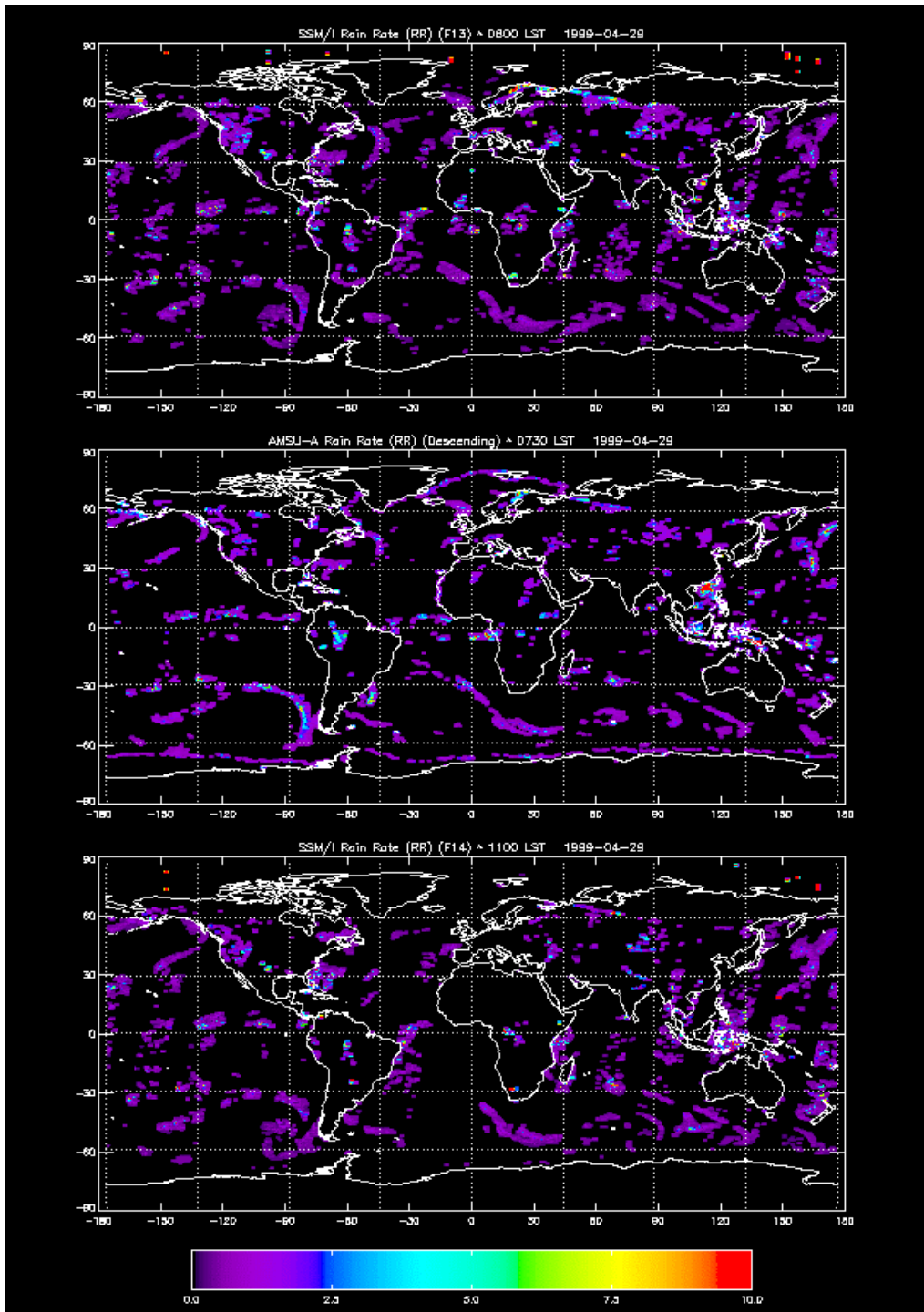


Figure 10. Daily rain rates (mm/h) for 29 April 1999 for SSM/I F-13 (top), NOAA-15 AMSU (middle), and SSM/I F-14 descending orbits (e.g., ~600 LST, ~730 LST, ~1000 LST, respectively).

Overall, the rain/no-rain areas between all three images (about 120 minutes apart) are fairly similar, meaning that the rain/no-rain screening worked essentially the same between the two sensor types.

Since AMSR will contain four channels at frequencies less than 19 GHz, we will also examine TMI (e.g., 10.7 GHz) and SMMR (e.g., 6.6 and 10.7 GHz) measurements to see whether improved screening can be developed using these frequencies. Techniques such as cluster analysis and principal components analysis will be employed. Upon the launch of ADEOS-II, we will utilize those available channels to finalize the screening portion of the rain over land module.

3.1.2.3 Instantaneous Land Rainfall – Rain Rate Determination

Because of the non-uniqueness in resolving proper hydrometeor profiles, based on SSM/I measurements, the use of physical retrieval algorithms over land has been limited. Although the proper surface rain rates may be retrieved by matching the observed Tb 's to model simulations, the intervening atmospheric cloud constituents are typically incorrect due to the lack of information available from the SSM/I. An alternative method to retrieve rain rate has been to calibrate the SI with ground-based radar measurements from the United States, Japan, and the United Kingdom (Ferraro and Marks, 1995). Specifically, the following relationship was found to work best for global applications:

$$RR(mm/hr) = 0.00513 \cdot SIL^{1.9468} \quad (10)$$

where RR is in mm/hr. Since these relationships increase rapidly for higher values of SIL , any retrieval above 35 mm/hr is set to 35 mm/hr. Although somewhat arbitrary, practice shows that this is the upward limit of rain rates retrievable from the 85 GHz measurements (e.g., the maximum mean rain rate that could exist in a 13 by 15 km FOV). Using the 10K minimum threshold for the SIL values, the minimum retrievable rain rate is approximately 0.5 mm/hr. This algorithm was implemented by FNMOC in 1995 as the operational SSM/I rain rate algorithm, and continues to operate in that capacity. In addition, the monthly derived rainfall from this algorithm (Ferraro, 1997) is used as a component of the GPCP blended analysis (Huffman *et al.*, 1996), is continually updated, is archived at the National Climatic Data Center (<http://www.ncdc.noaa.gov/ol/satellite/ssmi/ssmipproducts.html>), and can be examined interactively on the world wide web at <http://orbit35i.nesdis.noaa.gov/arad2/index.html>.

The AMSR instrument will contain slightly different frequencies than the SSM/I (e.g., 89.0 instead of 85.5 GHz), contain more information (e.g., 10 channels vs. 7), and will also have significantly higher spatial resolution. Because of these attributes, we feel that there will be an improved ability to retrieve hydrometeor profiles from the AMSR, although the ocean retrievals will still be more accurate. It is therefore convenient to have a physical basis for modifying SSM/I algorithms to suit the AMSR observations. To accomplish this, as well as to simplify the retrieval process, the AMSR precipitation team decided to use the same GPROF retrieval methodology as used for the ocean retrieval. Unlike the ocean component, however, the initial database of possible profiles was carefully selected to include only those profiles that fit the empirical relation given in Eq'n (13). The relationship of (13) was reproduced by selecting 36 profiles fitting (13) out of the several thousand profiles in the GPROF database (McCollum *et al.* 1999).

A sample comparison of daily, 0.25° rainfall estimates from global SSM/I data from March 8-10, 1999, is shown in Figure 11. As with all other days tested, there is very close correspondence between the GPROF rainfall estimates using the new profile database and the Ferraro (1997) algorithm estimates produced from (10), so it appears the GPROF algorithm using the new database is successful in producing similar rainfall estimates as the NESDIS algorithm for SSM/I data. The profiles selected for the SSM/I retrievals can then be used in a straightforward manner to compute the relations needed for the slightly different frequencies of AMSR. Resolution and additional channel measurement advantages can likewise be addressed through the cloud models and TRMM TMI and profiling radar measurements.

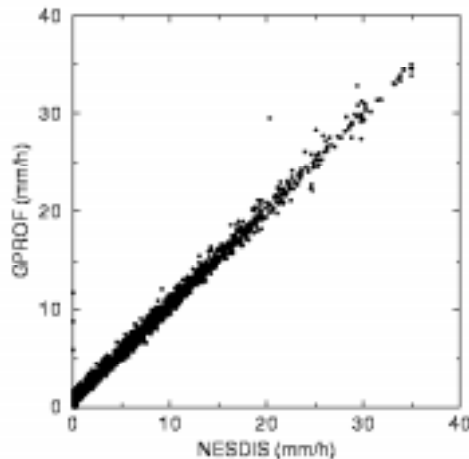


Figure 11: Comparison of 0.25° daily rainfall rates March 8-10, 1999) from the NESDIS empirical algorithm and from the GPROF algorithm with the new profile database.

3.1.2.3 Instantaneous Land Rainfall - Summary

For several years (1987 – 96), the SSM/I was the only passive microwave sensor that was operating. Beginning with TRMM (1997) and AMSU (1998), we are now in an era with multiple sensors in operation. Hence, the need for a “unified” retrieval algorithm that incorporates the best features of several existing algorithms, as well as one that is built in a framework that allows for continual enhancements is highly desirable. The AMSR rainfall team has adopted this philosophy and believes that the development of a unified land based retrieval algorithm for use with a variety of passive microwave sensors has several advantages. First, the same underlying physical assumptions (i.e., hydrometeor profiles, radiative transfer, etc.) are consistent. This allows for a more direct approach for evaluating and ultimately improving the retrieval process. These improvements can all be incorporated via the cloud model database and surface type/climate zone classification in the land retrieval module. The second advantage is that the module will be fully portable to other sensors, and will be suitable for operational/production use. This point cannot be stressed enough, as user friendly code is critical for a 24-hour a day, 7 day a week operation. Experience with SSM/I, TMI, and AMSU shows that even the smallest change to a software module can cause havoc in an operational environment! Finally, the implemented code will be the same for both land and water. This will greatly simplify the algorithm flow, thus enhancing our confidence that the code will work as intended.

3.1.3 Monthly Rainfall Accumulation

The level 3-rainfall algorithm is intended to produce monthly rain totals for 5°x5° degree boxes. Although it can be generated from level 2 products, it is not a simple average of the level 2 retrievals. We use the knowledge of the form of the probability distribution function for rainfall to help with the very high and very low rain rates that are difficult to measure and are poorly sampled. Over oceans we use a somewhat simpler level-2 algorithm than was discussed earlier. On monthly scales, the detailed needs of the hydrometeor structure is not as important as it is for the instantaneous rainfall, particularly in the emission regime. It is therefore possible to simplify the retrieval model. A simpler model, in turn, means that fewer assumptions are incorporated into the retrieval and results are more robust. Over land, emission schemes do not work and we will use the output of the previously discussed level-2 algorithm. Boxes that must be characterized, as mixed land/ocean will be classified first as ocean if sufficient rain is found in the box to meet the convergence criteria discussed in the subsequent section. Otherwise, a simple average of the land and ocean rainfall will be applied.

The embedded level 2 oceanic rain algorithm is based on the cloud and radiative transfer model (RTM) discussed in section 2. In this model we specify the distribution of hydrometeors, the atmospheric temperature structure, the water vapor profile and the surface reflectivity. Radiative transfer computations such as those shown in Figure 3 are performed. The result of such a computation can be reasonably well expressed as a brightness temperature as a function of rain rate and freezing level (height of the 0-degree isotherm). Ice is rarely a problem for frequencies near or below the 22 GHz water vapor line over the ocean. The relationships are thus robust indicators of the liquid water in the column.

Since the water vapor profile is specified in the model in terms of relative humidity, it is determined directly from the temperature profile which, in turn, is specified uniquely (in our model) as a function of the freezing level. (In recent improvements to the model, not yet implemented in the algorithm, the temperature profile is modified slightly by the latent heat release of the rain so the temperature profile is a function of both the freezing level and the rain rate (Tesmer, 1995). Thus the water vapor content is coupled directly to the

freezing level (and in the improved model to the rain rate). This enables us to determine the freezing level by using two frequencies with significantly different water vapor opacities. When using data from the SSM/I we use the 19.35V and 22.235V channels for a simultaneous solution for both freezing level and rain rate. The process is illustrated in Figure 12.

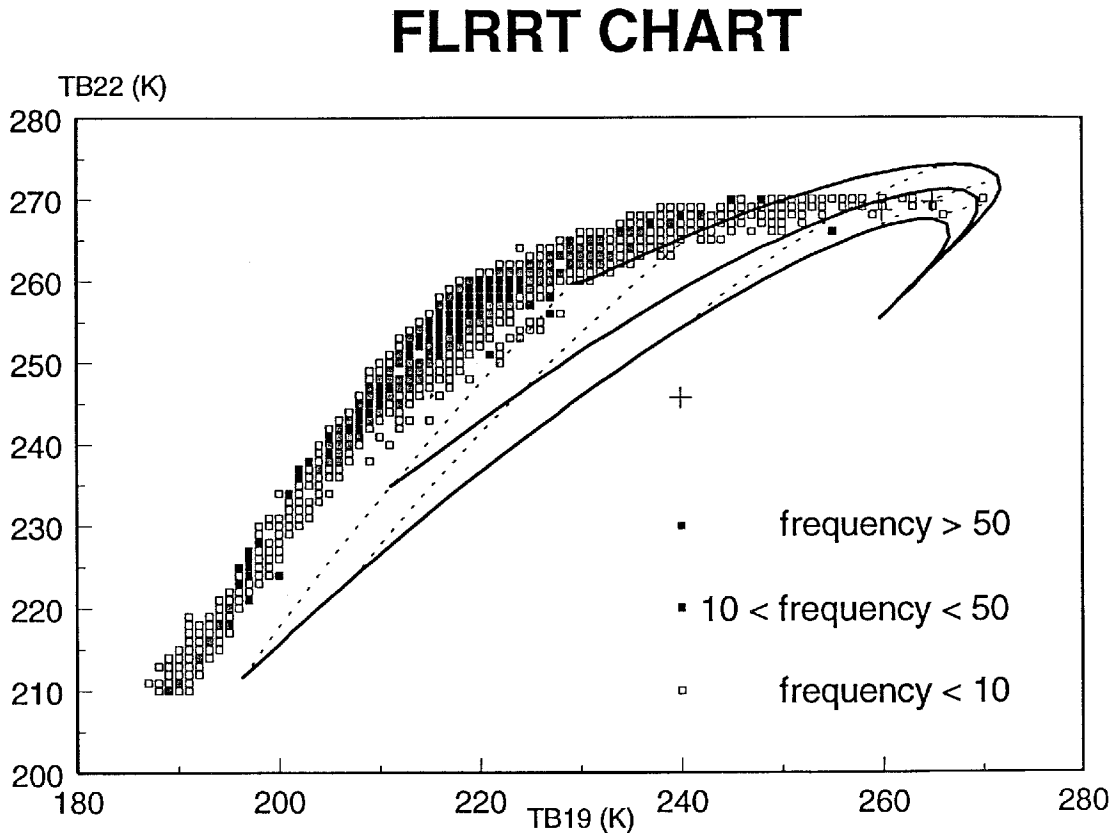


Figure 12: Rain Rate- Brightness Temperature relationships for two 19.35 Ghz channels of the SSM/I for several freezing levels. The heavy lines correspond to the vertically polarized channels and the lighter lines to the horizontally polarized channels.

Here we have plotted the frequency of occurrence of various values of the brightness temperatures in the 22V and 19V channels of the SSM/I for a 5° x 5° cell in the tropics. The solid lines are isolines of constant freezing level in this space. The top line corresponds to a 5 Km freezing level, the next 4 Km and the bottom one 3 Km freezing level. The dashed

lines are isolines of constant rain rate with 0 mm/hr being the leftmost followed by 1, 5, 10 & 15 mm/hr proceeding to the right. Thus a brightness temperature of 220K in the 19V channel and 240K in the 22V channel would correspond to a rain rate of 1 mm/hr and a freezing level of 4 km. Most of the observations are to the left of the 0-mm/hr line and indicate no rain and less cloud than is assumed in the model. (The cloud assumption corresponds to about 0.5 mm/hr). The observations to the right of the 0-mm/hr line mostly fall near the 5km freezing level, which would be reasonable for the tropics. The model assumes (unrealistically) uniform rain over the field of view. Since the isolines of constant freezing level are concave towards lower freezing levels, this inhomogeneity causes a slight underestimate of the freezing level at higher rain rates. (More on inhomogeneity in the next paragraph). The launch of TRMM has enabled us to look at this freezing level retrieval process. We have used the brightband as observed in the precipitation to provide a reliable measure of the freezing level within the radar swath (smaller than the TMI swath). When compared with the freezing level retrieved as described as above we found that the two tracked reasonably well with an RMS error of a few hundred meters and a bias of about 500 meters over a range of 3.5 to 5 km freezing levels. The source of the bias has been tracked down to errors in the water vapor absorption coefficient. Physically based corrections of these errors have reduced the bias to an undetectable level.

While there are many advantages to an absorption based algorithm, there are certainly difficulties as well. There are many assumptions in the model, some rather arbitrary, others likely to be violated in some degree at various places and times. However, it is clear that the dominant source of error in these retrievals is caused by the inhomogeneity of the rainfall within the field of view of the radiometer. The $Tb-R$ relationship is non-linear (in particular concave downwards) but the radiometer can only measure a linear average of the brightness temperature over the FOV. Thus, if the $Tb-R$ relationship is used at face value, an underestimate of the rainfall intensity will result, with the amount of the underestimate driven by the degree of the inhomogeneity. Since we don't know the structure within any individual FOV, we cannot correct for this underestimate in any particular case. We can correct for the average underestimate by a multiplicative factor, the Beam Filling Correction (BFC), so that the so-called "beam filling error" can be corrected to some degree in rainfall totals if not in individual observations. Clearly, a simple multiplier is likely to be too simple and there are significant uncertainties in what value of multiplier to use. Finding better ways of handling this problem remains a key research area.

It would be very tempting to compare retrieved rainfall totals with rainfall totals obtained by more direct means, often called "Ground Truth", and ascribe the discrepancy between the two to beam filling error. In so doing, we would essentially be throwing out our physical modeling and reverting to an empirical algorithm. Since we are working over the oceans, obtaining any "Ground Truth" is problematic in the extreme. A different approach has been taken. Radar observations of rainfall have been used as a measure of the structure of the rainfall while accepting that the radar calibration in terms of rainfall intensity may be suspect. The radar derived rain rates are converted into brightness temperature using a $Tb-R$ relationship, averaged over the presumed radiometer field of view, then finally converted back to rain rates using the same $Tb-R$ relationship. This "retrieved" rain rate will always be less than the "true" rain rate averaged over the field of view. The average value of their ratio is the beam filling correction for the size of the field of view and the climatic regime represented by the radar data set. This simulation approach examines the effect of rainfall structure in isolation from all other sources of error.

Recent research at Texas A&M has improved significantly on previous efforts in computing the BFC (Wang, 1996). The key to his research is that rainfall is variable in 3 dimensions and the radiometer attempts to average the effect of the rain over a volume. Since, at these frequencies, the absorption coefficient is essentially linear in the rain rate, the averaging done by the radiometer is done (almost) correctly along the line of sight (LOS); the BFC results from the other errors made in averaging in the other two dimensions (the plane perpendicular to the LOS). The traditional approach has been to take a 2 dimensional rain field derived from radar measurements, assume it is constant in the third dimension and use the resultant pseudo 3 dimensional rain field for the simulation. We have now obtained 3 dimensional rain fields from scanning airborne radars, which enable us to handle the 3 dimensional nature of the rain field more accurately. The rainfall is averaged along the line of sight (including the reflection off the ocean surface) before converting to brightness temperatures and integrating across the presumed antenna beam. This initial averaging step reduces the variability of the rain field and thereby reduces both the value and uncertainty of the BFC. For the 19 GHz channel of SSM/I the beam filling correction based on the traditional approach was about 1.8 but with the new computation it drops to about 1.4. The new computations also allow us to incorporate freezing level, frequency, and spatial resolution dependence in the BFC.

Another significant problem with rainfall retrievals is dynamic range. There are rainfall rates which are either too large or too small to be measured using a particular frequency.

For instance, at 19.35 GHz rain rates may be measured reasonably well over a range of roughly 2 to 20 mm/hr; at 10 GHz this range would shift to something on the order of 5 to 50 mm/hr and for 37 GHz 0.5 to 4 mm/hr. The exact value depends on the freezing level and the beam filling correction. Even with all 3 combined some of the rain will not be measured because it is outside of the dynamic range. Moreover, even if they can be measured, high rain rates will be poorly sampled because of their rarity. Because of this, we have taken the approach of using our knowledge of the form of the probability distribution function of rain to extrapolate the observations of the well-measured dynamic range into the poorly measured range. The algorithm discussed in Wilheit *et al.*, (1991) used a log-normal rainfall PDF with adjustable parameters to compute a histogram of brightness temperatures which was compared with the observed histogram of brightness temperatures; the parameters of the PDF were then adjusted to obtain agreement between the two. This algorithm is used operationally for the production of 5 degree by 5 degree by monthly rainfall totals for the Global Precipitation Climatology Project. Hong (1994) extended this to histograms of rain rate by developing a maximum likelihood estimator to compute the parameters of the PDF using only the valid dynamic range of the histograms. Redmond (1998) has developed a more stable formulation of the same concept. See Appendix I for a study of the impact and advantages of this Lognormal fitting process.

Figure 13 illustrates the proposed Level-3 rainfall algorithm, as it would be implemented for oceanic boxes. The brightness temperatures are passed through a filter to determine which ones could possibly represent rain. (This filter is the same one as in the level-2 profiling algorithm) Those for which significant rain is impossible are treated as a zero rain rate for the histograms to follow and also will be used for the instrument drift monitoring. Those pixels for which rain is possible will first be passed through an algorithm based on Figure 12 above to determine the freezing level (also used in the Level 2 algorithm). Using this freezing level, a number of rain rates can be computed, each valid over a specific dynamic range depending on the frequencies used. Those below the valid dynamic range are set to zero. Each of these rain rates is corrected for beam filling and then accumulated into histograms for the area and time period (nominally 5 degrees by 5 degrees by one month). One of the computed rain rates can then be used as a backup level 2 output as well. Currently, the rain rate is chosen on the basis of the largest rain rate retrieved at any pixel based on the logic that problems in the rain rate retrieval generally result in too low a rain rate. A more sophisticated logic for this choice is one of the tasks to be accomplished. Currently, a maximum likelihood estimator is used on a histogram of the chosen rain rate to compute the parameters of the lognormal distribution of rain rates.

Modular Oceanic Rain Rate Algorithm

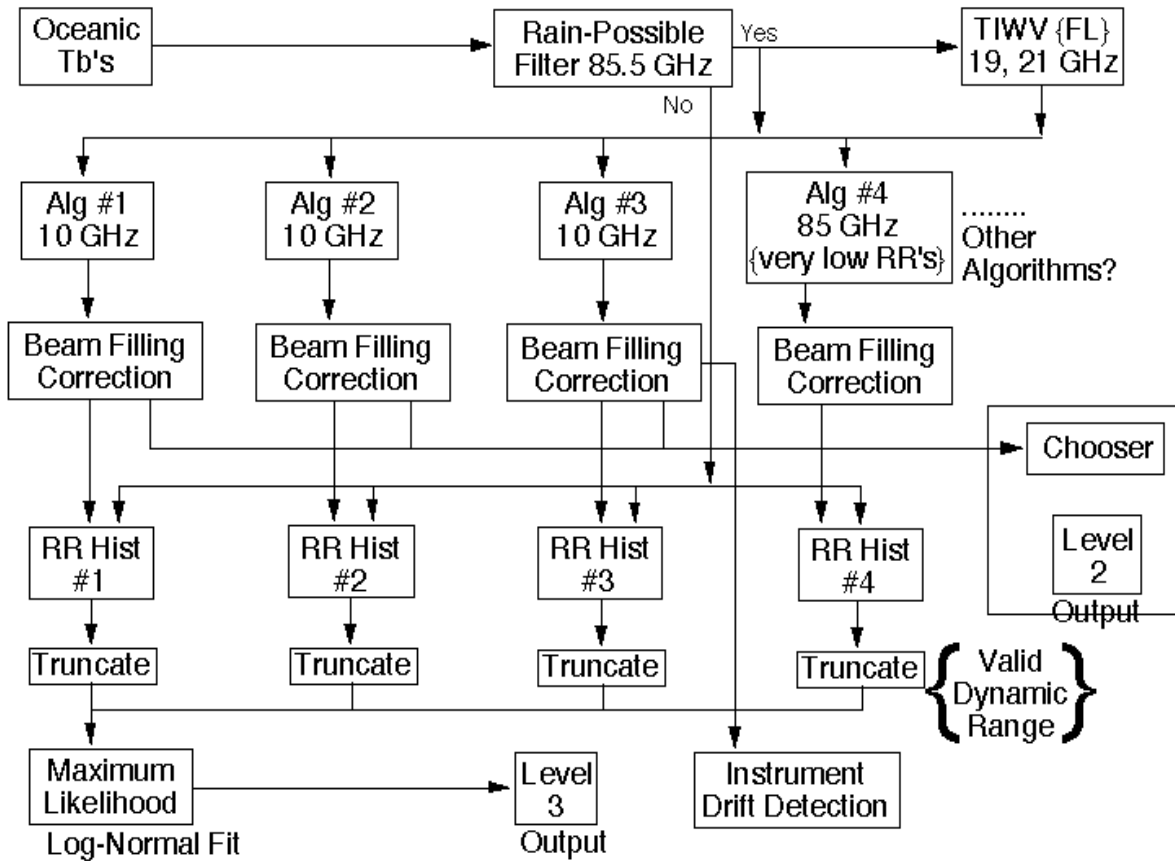


Figure 13: Level 3 conceptual flow diagram

At this point, the tests of the algorithm as described have not been especially successful. The problem seems to stem from an error in the zero rainfall point. The computer code includes the option of doing the fit in brightness temperature space rather than in rain rate space. This is the approach that has been used for a decade on the Global Precipitation Climatology Project (GPCP). A key feature is that the GPCP version solves explicitly for the zero rain brightness temperature thus eliminating the zero rain offset problem. The GPCP version has been applied to the TMI data and appears to be the best performing algorithm as of now. In principle, the version described above should work better. We now understand how to cancel out the zero rain rate error and are in the process of assembling a new version for testing. For now the GPCP version will be the baseline until we have a convincing demonstration that the “improved” version is truly an improvement.

3.2 VARIANCE AND UNCERTAINTY ESTIMATES

Despite the clear physical connection between increasing microwave brightness temperatures and the liquid water content in clouds, there are, nevertheless, a number of uncertainties. The most obvious of these is the need for an estimate of the rain layer thickness, the freezing level in the model discussed. Even if an acceptable estimate of the freezing level is available, the rain layer thickness may be less as in the case of warm rain or greater in convective cores. Perhaps not as obvious, but of great importance, is the effect of inhomogeneous rainfall below the resolution of the satellite. Due to the concave downward nature of the relationships shown in Figure 3 (particularly for the frequencies where emission dominates), homogeneous rainfall with the same intensity as an inhomogeneous field will have warmer Tbs . This effect, if not properly accounted for, will lead to consistent low biases in emission based rainfall estimates.

At the wavelengths useful for emission based rainfall estimates, water vapor is a significant and variable contributor to the brightness temperature. Some algorithms use additional observations near the 22.235 GHz water vapor line (23.8 GHz for AMSR) to estimate the water vapor, but the needed ability to model the brightness temperatures accurately within a field of view with a varying rainfall intensity and perhaps some scattering by frozen hydrometeors is uncertain at best. Another potential source of error is the non-precipitating component of the cloud. Spectrally, the cloud has no useful difference from the rain so that multi-frequency approaches have no promise for discriminating between clouds and rain. An independent estimate, or at least an upper limit, is needed to eliminate this contribution to the brightness temperatures.

Wind at the ocean surface also increases the brightness temperatures somewhat. However, given the other serious uncertainties in the rainfall retrieval problem, the wind speed contribution must be considered as minor. A great deal of progress must be made before the wind speed error will be a sufficiently important element in the error budget to warrant serious attention.

Scattering-based retrievals have even more severe uncertainties. This uncertainty is dominated by the lack of a consistent relationship between the frozen hydrometeors aloft and the liquid at lower altitudes. There is evidence, however, that there is at least a

statistical consistency within a given climate regime. The assumption of a Marshall-Palmer distribution of hydrometeors in the earlier calculations was strictly for illustrative purposes. The reality is much more complicated. Some of the algorithms attempt to deal with the size distribution by the use of storm scale models with (hopefully) realistic ice phase physics packages. The shape distribution is yet another matter. Few of the frozen hydrometeors could be characterized as spherical. Indeed, few could be characterized as any shape for which the solution of Maxwell's equations for the scattering cross sections is tractable. Thus, quantitatively accurate treatment of scattering by ice is extremely problematic.

Another problem encountered by scattering based retrieval algorithms is that rainfall (and associated ice) is not the only scatterer of microwave radiation. Snow cover, when the liquid water content is negligible, is a strong scatterer. The snow cover in the mountains and the icecaps of Greenland and Antarctica is clearly visible as low brightness temperatures in the 85.5 GHz channel of SSM/I. Very dry sand as in the desert areas can also scatter significantly and appear to be rainfall. Careful screening procedures, which tend to be empirically determined, are needed to reduce such ambiguities.

The goal of the AMSR rainfall algorithm has been to develop algorithms that are as physically based as possible for reasons already outlined. Physically based algorithms have the advantage that their applicability to various meteorological regimes can be tested and verified by examining the physical assumptions made in the models. Despite the clear connection between the physical assumptions and retrieved rainfall, however, there have not been, until recently, any serious attempts by the passive microwave community to use these relationships to establish an error model. Instead, most investigators have been content to compare retrieved rainfall to those obtained from ground based radars or rain gauge networks. By resorting to empirical methods in the error estimates, unfortunately, important strengths of the physically based algorithms have been lost.

Modeling of errors is a complex subject. Complications arise because the uncertainty in the retrieved rainfall is not simply propagation of measurement uncertainty but also of uncertainties in the assumptions regarding the nature of precipitation itself. Recent studies, however, have begun the process of constructing error models by examining the largest uncertainty in many of the physical models - the homogeneous rainfall assumption (see Kummerow, 1996). Four months of TOGA-COARE shipborne radar data were used to describe the horizontal characteristics of rain. The vertical hydrometeor structures needed

to simulate the upwelling T_b were taken from a dynamical cloud model. Radiative transfer computations were performed using a fully three-dimensional Monte Carlo solution in order to test all aspects of the beamfilling problem. Results show that biases as well as random errors are due to a number of assumptions, not merely the non-linear T_b to rainfall relations. Figure 14a shows the variability of rainfall for 24-km footprints commensurate with the AMSR 19 GHz brightness temperature. Figure 14b shows the effect of the uncertainty in the rainfall distribution upon the computed T_b at 19 GHz. As can be seen from these results, large errors are possible for individual pixels. These errors, however, tend to be random in nature and reduce quickly as area/time averages are taken. More work is needed in that study to bring together rainfall characteristics from radars around the world. TRMM radars will provide these data for tropical environments. A comprehensive validation program for AMSR must also consider radars in the extra-tropics in order to develop a global model for uncertainties due to the rainfall inhomogeneity. One of the major goals of the Kwajalein Experiment, currently being planned under the aegis of TRMM and to be executed during the summer of 1999, will be to get additional data sets to address this problem.

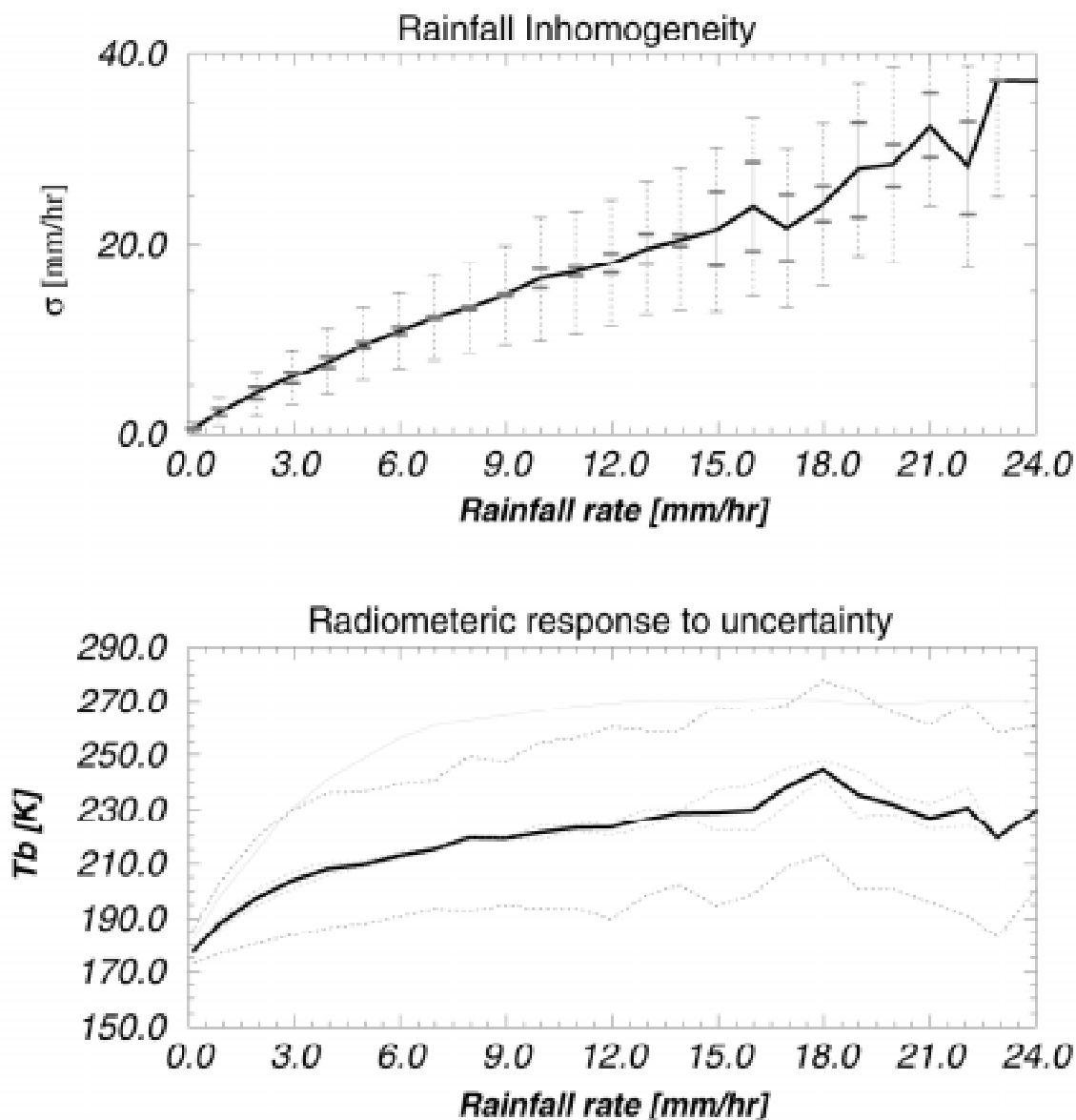


Figure 14: Variability of rainfall and effect upon 19 GHz T_b . Top panel shows relationship between rainfall and rainfall inhomogeneity. Red error bars are for monthly variations. Black dashed error bars are for instantaneous variations. Bottom panel shows the effect of uncertainty in the inhomogeneity upon the computed 19 GHz T_b . Red dashed lines represent uncertainty due to monthly variations. Black dashed lines represent uncertainty due to instantaneous variations in the inhomogeneity. The green line corresponds to homogeneous clouds.

A second component of the uncertainty is the unknown vertical structure of the precipitation. While the oceanic level 2 retrieval algorithm specifically tries to capture the vertical structure, it cannot differentiate two vertical hydrometeor profiles if these have identical Tb signatures. This problem can be studied using the cloud model database. Different profiles with similar Tb at all the channels (non-uniqueness problem) can be compared in order to derive an error estimate. To construct a realistic error model, however, it is further necessary to determine the probability that specific non-unique profiles are observed in nature. Again, the results obtained from the TRMM mission will be invaluable to construct this portion of the error model. Of greatest value will be the profiles as derived from the TRMM radar. Also useful, however, will be statistics concerning the vertical reflectivity structure observed by the TRMM and other ground based radars at higher latitudes.

Other components receiving attention are the uncertainty in the computed Tb due to uncertainties in the drop size distributions (see McKague *et al.*, 1996). While unknown drop sizes play a relatively minor role in determining Tb in the emission regime, they become increasingly important as scattering by raindrops begins to dominate. Uncertainty in time and space averages due to the sampling of the characteristics of the satellite (Bell, 1987; Bell *et al.*, 1990; North *et al.*, 1993) is another area that has received attention recently. Most of the above studies, however, must be considered as being in their early stages. A comprehensive error model for microwave rainfall retrievals is still beyond our immediate grasp.

The main thrust of the rainfall research in the AMSR precipitation team will be the development of valid error models. To insure that such activities can take place, the EOS/AMSR team has taken an active role in the planning of validation experiments. Some of the steps outlined below should be taken as soon as practical - others must obviously wait until the instrument is taking observations.

3.2.1 Calibration/Validation

When discussing calibration, one must separate between sensor calibration and algorithm calibration as either one would affect the geophysical products. While sensor calibration is perhaps more in the domain of the Level 1 and the Ocean Parameter Suite algorithm, it is nonetheless important for rainfall retrieval purposes to begin by verifying that the sensor is operating correctly. Particularly, since rainfall can cause very warm Tb to be observed, it

is particularly important to verify that this end of the calibration and not just the cold end are operating correctly. Carefully calibrated aircraft radiometers flying over land with a uniform warm background can be used for this purpose.

Algorithm calibration is an entirely different matter and one which, will not be applied to the AMSR rainfall products. As discussed at the onset of this report, the rainfall package has made deliberate attempts, wherever possible, to avoid arbitrary calibrations. This is particularly true in the case of rainfall which is as difficult to measure from ground based platforms as it is from space. Instead, we will employ surface observations to carefully examine the behavior of the spaceborne algorithms under different conditions. If deficiencies are found, we will attempt to understand the physical reasons for these deficiencies and correct them rather than applying tuning coefficients, which may lead to locally better results but have no basis in global applications.

Comparisons with ground based radars are necessary to check for egregious errors and to monitor overall performance. For comparisons of the AMSR rainfall, both instantaneous as well as monthly estimates are required. It is currently assumed that AMSR will take advantage of the opportunities left behind by the TRMM mission by keeping key TRMM validation sites operating into the AMSR era. The TRMM network, consisting of ten sites shown in Figure 15, will all have received tremendous attention during the TRMM era and are likely to be best sites available at that time. Recent work by Li *et al.* (1998) using SSM/I data has led to the development of a new method for assessing the algorithm and sampling errors, and will be utilized by the AMSR rainfall team. Finally, it is important that the AMSR precipitation team pursue additional extra-tropical sites to participate in this effort so that a more globally representative dataset is available. The WSR-88 operation in Eureka, CA has been identified as a potential candidate with both ocean and land coverage.

means is that it is not critical for this study that the radar calibration be accurate to less than 1 dBZ even though a 1 dBZ error translates into rainfall errors of approximately 15%. Moreover, effects such as variable drop size distributions and radar attenuation can be ignored since only the rainfall in the vicinity of the pixel in question is needed. Thus, the variability statistics can be seen to be far more robust than the rainfall estimation. The AMSR validation effort will concentrate on these kinds of comparisons that test the basic physics within an algorithm, rather than the traditional method of taking “ground truth” to be sacred and adjusting all spaceborne observations to match.

3.2.2 Physical Validation

Ultimately, we cannot rely from incomplete statistics from a few coastal radars, and must go to the physical validation approach for the oceanic rainfall. In order to have a physical validation approach, it is first necessary that algorithms be physically-based; we have gone to great pains to assure that the AMSR oceanic rainfall algorithms are, in fact, physically based. Next the dominant sources of uncertainty must be identified. If one considers climatological products, rainfall totals over a space-time volume, then sampling is a major source of error; we simply do not see all the rain and must infer the occurrence of rainfall between the observations. In practice this will always be the dominant source of error. If additional observation capability is added the users will immediately demand finer space-time resolution, so that the sampling error remains at the maximum tolerable level.

We plan two approaches for estimating the sampling error. First the data taken for the Ground Truth approach will be sub-sampled to coincide with the satellite sampling observations. The rainfall totals derived from this sub-total will be compared with totals from the complete data set. Adjustments will have to be made for the areal coverage of the radar not coinciding with that of the satellite, but these will not prove difficult.

Another approach that can be applied globally is to make two separate satellite derived estimates based on alternate days. (e.g. odd and even days of the year) If the area covered by each estimate is doubled, the sampling will remain constant. This approach will estimate all random sources of error rather than just the sampling error. The impact of the other random sources of error can be estimated by comparing with the sampling error estimates derived from the radar data. Thus the sampling error estimated at a few radar locations can be spread globally.

For the instantaneous rainfall error there are three major sources of error:

- 1) Beam Filling Error
- 2) Vertical distribution of Hydrometeors
- 3) The freezing level retrieval

The beam filling correction is done by simulation. It may either be incorporated into the Brightness Temperature - Rain Rate (TR) relationships or as a multiplicative factor. The difference is a mechanical choice; the underlying concept is the same. To date these simulations have been based on limited data sets from either airborne radar or hydrodynamic Cloud Resolving Models (henceforth "CRM's") of which Tao's model is a well-known example. The relative advantages and disadvantages of each approach are fairly obvious. In neither case do we have a sufficiently wide range of conditions to be comfortable with the corrections or even estimates of the uncertainty of the corrections. It is not practical to get enough airborne radar data to cover the range of possibilities adequately. The CRM could be run for as many situations as we chose, but we have less confidence that the length scales are really correct. What is needed is to get reliable statistics derived from radar data for a few dozen locations in the tropics and extratropics in various seasons. We recommend the use of the new NASA 10-cm dual polarized radar for this purpose. We further recommend that these observations be coupled with sounding such that CRMs can be initialized and their properties compared to the observations. The CRM's may need to be refined to achieve the same results over the range of conditions. Having models in which we have confidence is critical not only for advances in beamfilling corrections, but latent heating inferences as well.

The vertical distribution of hydrometeors is a particularly difficult parameter to observe remotely, and different CRM's still give widely disparate pictures of the liquid content in the mixed phase region just above the freezing level. This, in turn, gives widely varying effects of scattering in this region. The bright band region is of special interest. In the bright band region, the region just below the freezing level where the snow melts to form rain drops, the radiometer and radar communities model the attenuation differently. The radiometer community, on the basis of limited evidence, treats the attenuation as being the same as in the rain area below whereas the radar community treats the bright band as having twice the attenuation of the rain below.

Aircraft penetrations with appropriate instruments are the best way to settle the questions. Cloud particle imaging systems (e.g. PMS probes) provide phase and density information. Upward viewing microwave radiometers provide integrated measurements of the attenuation above the aircraft. Once again, having soundings to go with the measurements will allow the running of CRM's to compare with the observations and allow the refinement of these models so they can be used to cover a wider range of conditions than is accessible with a reasonable number of aircraft hours.

If the PM-1 satellite had a radar, it would be straightforward to validate the freezing level retrieval, and by implication, the thermodynamic assumptions of the RT models. With TRMM data, the retrieved freezing levels are being compared with freezing levels inferred from the bright band in the radar data. This will nearly suffice for the AMSR freezing levels in the tropics. It will be important to extend this validation to higher latitudes (lower freezing levels). The mobile ground based radar, if scanned appropriately for this purpose, can partially achieve this goal by making careful measurements of the bright band height. Airborne radar in rain under the PM-1, and direct aircraft penetrations of convective systems may be needed to obtain the freezing level when no bright band is present.

During 1998, the CAMEX experiment was flown in and around Florida. Many of the required sensors were on the various aircraft involved in the campaign. Although the aircraft time was divided among a wide variety of issues, at least a preliminary look at several of the PV issues was taken. The analysis of the data has not proceeded sufficiently to say just how much progress was made.

During 1999, under the aegis of TRMM, the KWAJEX experiment will be flown in the neighborhood of Kwajalein Atoll. The experiment is devoted to addressing the PV issues discussed above. There will be three aircraft involved to cover the vertical range of the precipitating systems and to simulate the satellite observations, but at higher spatial resolution. This should provide a very good first order estimate of the uncertainties contributed by the major elements in the error budget. While a single location is unlikely to provide final answers, it will permit a much more refined and focussed set of questions to be addressed in future experiments that must cover a variety of rainfall regimes. Both the CAMEX and KWAJEX experiments were supported by non-Eos funding and would have happened in the absence of AMSR.

We project that two aircraft campaigns will be needed to extend the aircraft work done under TRMM. First we must get high latitude (low freezing level) oceanic observations. A deployment to the North Pacific/ Gulf of Alaska or South Pacific/Punta Arenas during the winter would be climatologically appropriate, with the Gulf of Alaska being logistically simpler. The aircraft and payload complements of the CAHMEX would represent a first estimate of the observational requirements. Analysis of the CAMEX and KWAJEX data will refine these requirements. Given the lifetimes of synoptic scale systems and the dense satellite coverage at high latitudes, it should be possible (and is clearly desirable) to have the bulk of the observations within a few hours of a satellite observation.

Depending upon the outcome of the high-latitude experiment, we feel that it is prudent to plan for a second aircraft campaign, which is similar to the first, but concentrates upon the area of poorest agreement between theory and observations. While it is possible to speculate about where such disagreement might be most serious, we think this location for the experiment should be deferred until data is available. Details about the planning of AMSR-E validation campaigns can be found in the AMSR Validation Plan.

3.3 PRACTICAL CONSIDERATIONS

3.3.1 Numerical Computation Considerations

A schematic of the algorithm is included in Figure 16. After ingesting a granule of data, the algorithm goes through a quality control procedure and classification into either possible rain, clear sky or indeterminate pixels. Over oceans, the classification consists essentially of a cloud liquid water retrieval. When the cloud liquid exceeds a nominal threshold, the pixel is said to be potentially raining and the rain portion of the retrieval is invoked.

The three components of the algorithm, as mentioned before, are all running in either operational or semi-operational mode on moderate size workstations (much smaller than those considered by the AMSR SCF). As such, we see little or no problem from the computational perspective. On an SGI Indigo 2 workstation, the rain algorithm can process 1 month of SSM/I data in approximately 12 hours. Even allowing for the data rate of AMSR which is approximately 10 times higher than SSM/I, a small workstation would still be capable of producing rainfall estimates in a timely fashion.

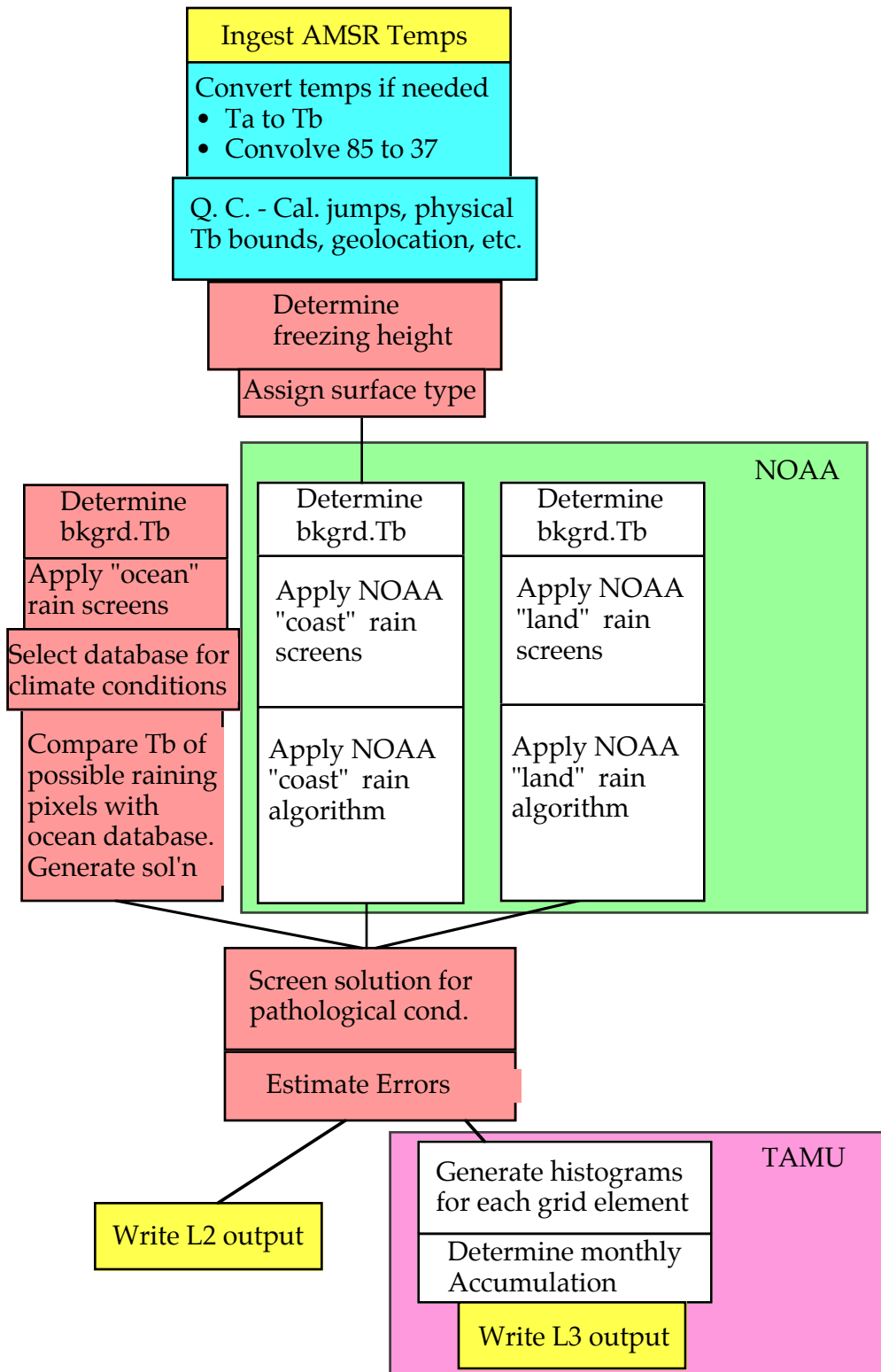


Figure 16: Schematic of the combined retrieval algorithm.

Recent comparisons of Level 2 accumulated rainfall from TRMM TMI generated by the GPROF algorithm over ocean and the Level 3 ocean algorithm are shown in Figure 17. As can be seen, the differences are quite small, amounting to less than a few percent when globally averaged. This result gives credibility to our approach. The Level 2 algorithms strive to produce the best instantaneous product. In doing this, however, a number of non-linear assumptions are introduced. By ignoring the instantaneous rain retrieval problem, the Level 3 algorithm inherently is more stable. The fact that they agree in their monthly accumulations only demonstrates that one approach is not better than another – they are merely optimized for their respective purposes.

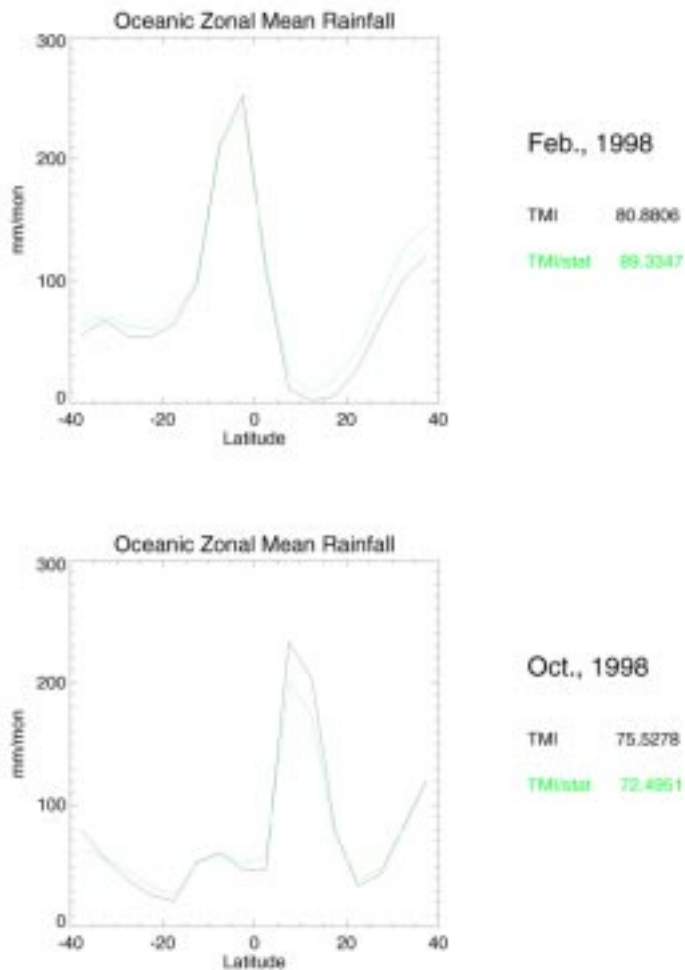


Figure 17: Zonal average rainfall over ocean derived from the AMSR Level 2 (TMI) and Level 3 (TMI-Stat) algorithms applied to TRMM TMI data.

3.3.2 Programming/Procedural Considerations

The algorithm, as will be implemented for EOSDIS is a straightforward combination of the instantaneous and monthly components - both of which have been coded and delivered to the TRMM Data and Information System (TSDIS) in April of 1996. In planning for the TSDIS delivery, many of the “programming and procedural” issues have already been addressed.

The oceanic instantaneous rainfall retrieval (GPROF) will serve as a backbone for the merged algorithm. The general flow of the retrieval algorithm was agreed upon at the second Precipitation Intercomparison Project (PIP-2) workshop. The code design is modular in nature and designed in such a way that different pieces of algorithm from various investigators could be easily merged. As such, GPROF is fully capable of accepting the land algorithm developed by NOAA. Integration and testing will be performed at GSFC. It is not expected to require more than 1 day. Likewise, the ingest of AMSR level 1 data is fully isolated (within an “ingest” subroutine). Writing this new interface does not require any major effort assuming that the AMSR data format is constant and not changing with each EOS-HDF release. The entire source code as well as external files will be delivered to the AMSR SCF.

The Level 2 algorithm expects two file names from the AMSR SCF scheduler: The input file name from which to read the level 1 data, and the output file name to which to write the geophysical parameters. There are 7 external files, which are called by the Level 2 algorithm. These files are constant - they are not expected to change during the mission except during algorithm upgrades. The first five are database files containing cloud structures for the oceanic component. The other three files consist of: 1) a custom land/sea database needed only if this information is not supplied with the level 1 data; 2) A freezing level conversion lookup table; 3) A climatological freezing level which can be used over land or as backup. All files are FORTRAN formatted files. [Note that the working assumption here is that one input file (granule) represents one orbit of data. However, this is not a requirement. The algorithm will process data of any given input length].

Level 3 algorithms tend to be more problematic because a long sequence of data must be ingested before monthly products can be computed. To simplify the operational requirements of this algorithm, the Level 3 algorithm is divided into two components. The

first accumulates the required statistics for each orbit. This step will be accomplished as an additional output subroutine in GPROF above. The output file (which can be considered an intermediate product) must also be given a name. Thus, in order to handle the Level 3 intermediate data processing, the statement that Level 2 algorithm needs two (input, output) file names must be amended to: The Level 2 algorithm needs three file names - the input file name, the output file name, and the intermediate file name in which to store the Level 3 temporary aggregate parameters. These intermediate files, fortunately, are generally small and cause no real problems if kept for periods of about 1 month. Once the scheduler determines that the data for an entire month has been processed at the Level 2, the scheduler must kick off the Level 3 algorithm, passing the appropriate intermediate file names to the Level 3 accumulator. While the algorithm flow is not terribly elegant, it is simple and allows for simple recovery should problems occur. The only complication occurs for orbits which cross the month. Since portions of the file have to be added into two separate monthly accumulation, the scheduler must keep track of these temporary files in order not to delete them prematurely.

The algorithm input consists of brightness temperatures, latitude, longitude, time and land/ocean background as supplied by the Level 1C AMSR product. No Metadata is explicitly required. No external data sources except those files supplied with the algorithm are needed to execute the rainfall algorithm.

3.3.3 Quality Control and Diagnostics

The first step in quality control will be the visual examination of the rainfall products on various time and space scales to insure that the rainfall maps are consistent with our physical understanding of climate, and that no egregious errors are being made. We will further compare the retrieved rainfall with rainfall estimates from ground based radars, paying particular emphasis on the correlation between the two. Biases will be considered, but it should be clear that ground based radars often have their own biases so that quantitative conclusions are often difficult.

Replacing existing AMSR algorithms with completely new algorithms that are perceived to be slightly better at any given time may temporarily improve our statistics. It may at the same time, however, introduce any number of new problems. The AMSR precipitation

team will instead rely most heavily on algorithms improvements that can be linked to algorithm shortcoming that are demonstrable and correctable. We intend to encourage the critical evaluation not only of the final rainfall product, but of each of the intermediate assumptions. When a particular assumption is found to be deficient, we will encourage better procedures in such a way that the operational algorithm and our understanding both mature in unison.

3.3.4 Exception Handling

Most exceptions must be handled by the Level 1 algorithm. In this section we emphasize only those items which the AMSR precipitation team believes is significant for Level 2 and Level 3 processing. By far the most likely as well as the most troublesome exception that must be dealt with is that of missing data. Missing data can be classified and treated according to the amount of information missing:

- a) Some fields are missing at the pixel level: The quality control portion of the algorithm checks the required fields and makes decisions regarding the usefulness of the data. If critical fields are missing, then the Quality Control subroutine will simply set the output parameters of those pixels to missing. Should the information be irrelevant to the Level 2 processing, then the retrieval will proceed.
- b) Entire pixels are missing: The retrieval algorithm is expecting a fixed number of pixels per scan. Missing pixels must therefore be inserted as “missing” pixels at the Level 1 processing. If the number of pixels per scan line is not equal to the expected number then the program will terminate with the appropriate error message.
- c) Entire scan line is missing: The retrieval relies on neighboring pixels within a swath to compute certain rainfall statistics. If scans are missing, the code expects these scans to be present with “missing” values. The Quality Control subroutine checks for the time between successive scan lines. If the time between consecutive scan lines is not the expected 1.5 seconds, the program will terminate with the appropriate error message.
- d) The entire orbit is missing: The Level 2 algorithm is not affected by this condition. For Level 3 purposes, however, the group feels more confident if orbits with the appropriate Metadata but no scan data are added to the system. This allows the Level 3 algorithm to verify that the necessary input files have been received. It further allows both the Level 2 and Level 3 algorithm to distinguish the two conditions: a) No data was available; from b) data is available but could not be processed because of unexpected problems in the operational system.

Other exceptions that are planned for consist of the following:

- a) Insufficient orbits at the Level 3 algorithm: If the minimum amount of data needed to compute credible monthly estimates is not met, the monthly product will be set to missing.
- b) Abnormal program termination: Unless the program termination code is the normal termination, the appropriate error message will be sent to the operator. While we hope this never happens, the three P.I.s of the rainfall product will be prepared to take corrective action as needed.
- c) Files not found: The program will terminate and the appropriate error message will be sent to the operator.
- d) Fatal computation error: This will result in an abnormal termination.
- e) Non-fatal computation error: Appropriate error message will be sent to operator who will halt processing until problem can be resolved.

4.0 REFERENCES

- Anagnostou, E. N. and C. Kummerow, 1997: Stratiform/Convective Classification of Rainfall Using SSM/I 85 GHz Brightness Temperature Observations. *J. Atmos. and Ocean Tech.*, **14**, 570-575.
- Atlas, D., and C. W. Ulbrich, 1978: Path- and area-integrated rainfall measurement by microwave attenuation in the 1-3 cm band. *J. Appl. Meteorol.*, **16**, 1322-1331.
- Bell, T. L., 1987: A space-time stochastic model of rainfall for satellite remote sensing studies. *J. Geophys. Res.*, **92**, 9631-9643.
- Bell, T. L., A. Abdullah, R. L. Martin, and G. R. North, 1990: Sampling errors for satellite-derived tropical rainfall: Monte Carlo study using a space-time stochastic model. *J. Geophys. Res.*, **95**, 2195-2206.
- Berg, W., and R. Chase, 1992: Determination of mean rainfall from the special sensor microwave/imager (SSM/I) using a mixed lognormal distribution. *J. Atmos. Oceanic Tech.*, **9**, 129-141.
- Chandrasekhar, S., 1960: Radiative Transfer. Dover Publications, New York, 393pp.
- Ferraro, R.R., N.C. Grody, and G.F. Marks, 1994: Effects of surface conditions on rain identification using the SSM/I, *Rem. Sens. Rev.*, **11**, 195-209.
- Ferraro, R.R. and G.F. Marks, 1995: The development of SSM/I rain rate retrieval algorithms using ground based radar measurements. *J. Atmos. Oceanic Technol.*, **12**, 755-770.
- Ferraro, R.R., E.A. Smith, W. Berg, and G. Huffman, 1996: A review of screening techniques for passive microwave precipitation retrieval algorithms. *J. Atmos. Sci.*, **55**, 1583-1660.
- Ferraro, R.R., 1997: SSM/I derived global rainfall estimates for climatological applications. *J. of Geophys. Res.*, **102**, 16,715-16,735.
- Foot, C. B., and P. S. duToit, 1969: Terminal velocity of raindrops aloft. *J. Appl. Meteorol.*, **8**, 249-253.
- Goody, R. M., and Y. L. Yung, 1989: Atmospheric Radiation. Oxford University Press, pp. 330-337.
- Grody, N.C., 1991: Classification of snow cover and precipitation using the Special Sensor Microwave/Imager (SSM/I). *J. of Geophys. Res.*, **96**, 7423-7435.
- Gunn, K. L. S., and T. U. R. East, 1954: The microwave properties of precipitation particles. *Quart. J. Royal Met. Soc.*, **80**, 522-545.
- Hollinger, J. P., J. L. Pierce, and G. A. Poe, 1990: SSM/I instrument evaluation. *IEEE Trans. Geosci. Rem. Sens.*, **GE-28**, 781-790.

- Hong, Ye, 1994: Retrieval of monthly rainfall over the oceans from the Special Sensor Microwave Imager (SSM/I); Ph.D. Thesis, Department of Meteorology, Texas A&M University.
- Hong, Y., C. Kummerow, and W. S. Olson. Separation of Convective/Stratiform Precipitation Using Microwave Brightness Temperature. *J. Appl. Meteorol.* (conditionally accepted).
- Houze, R. A. Jr., F. D. Marks, and R. A. Black, 1992: Dual-aircraft investigation of the inner core region of hurricane Norbert. Part II: Mesoscale distribution of ice particles. *J. Atmos. Sci.*, **49**, 943-962.
- Huffman, G.J., R.F. Adler, P. Arkin, A. Chang, R. Ferraro, A. Gruber, J. Janowiak, A. McNab, B. Rudolf, and U. Schneider, 1996: The global precipitation climatology project (GPCP) combined precipitation data set. *Bull. Amer. Meteor. Soc.*, **78**, 5-20.
- Jackson, J. D., 1962: Classical Electrodynamics. John Wiley and Sons Inc., New York, pp. 216-220.
- Jung, H. J., 1980: The determination of rainfall rates from satellite measurements of the thermal microwave emission. *Contrib. Atmos. Phys.*, **53**, 366-388.
- Kummerow, C., R. A. Mack and I. M. Hakkarinen, 1989: A self-consistency approach to improve microwave rainfall estimates from space. *J. of Appl. Meteor.*, **28**, 869-884.
- Kummerow, C., 1993: Radiative Transfer Model Comparisons for Passive Microwave Frequencies. *J. Geophys. Res.*, **98**, 2757-2765.
- Kummerow, C., and L. Giglio, 1994: A Passive Microwave Technique for Estimating Rainfall and Vertical Structure Information from Space, Part I: Algorithm Description. *J. Appl. Meteorol.*, **33**, 3-18.
- Kummerow, C., W. S. Olson and L. Giglio, 1996: A Simplified Scheme for Obtaining Precipitation and Vertical Hydrometeor Profiles from Passive Microwave Sensors. *IEEE Trans. on Geosci. and Rem. Sen.*, **34**, 1213-1232.
- Kummerow, C., 1996: Beamfilling Errors in Passive Microwave Rainfall Retrievals. *J. Appl. Meteor.*, (submitted)
- Li, Q., R. Ferraro and N.C. Grody, 1998: Detailed analysis of the error associated with the rainfall retrieved by the NOAA/NESDIS SSM/I Rainfall Algorithm: Part I. Tropical oceanic rainfall. *J. Geophys. Res.*, **103**, 11,419-11,427.

- Lorenc, A. C., 1986: Analysis methods for numerical weather prediction. *Quart. J. Royal Met. Soc.*, **112**, 1177-1194.
- McKague, D. K. F. Evans, and S. Avery, 1996: Assessment of the effects of drop size distribution variations retrieved from UHF radar on passive microwave remote sensing of precipitation. *J. Appl. Meteor.* (submitted).
- McCollum, J.R., A. Gruber and M.B. Ba, 1999b: Discrepancy between gauges and satellite estimates of rainfall in equatorial Africa. *In press, J. Appl. Meteor.*
- McCollum, J.R., R. Ferraro, C. Zhou, C. Kummerow, Y. Wang, 1999b: The EOS-PM1 AMSR land rainfall algorithm. *Submitted, J. Geophys. Res.*
- Mie, G., 1908: Beiträge zur Optik Trüber Medien, speziell kolloidaler Metalösungen. *Ann. Phys.*, **26**, 597-614.
- Mugnai, A., E. A. Smith, and G. J. Tripoli, 1993: Foundation of physical-statistical precipitation retrieval from passive microwave satellite measurements. Part II: Emission source and generalized weighting function properties of a time dependent cloud-radiation model. *J. Appl. Meteor.*, **32**, 17-39.
- North, G. R., S. S. P. Shen and R. Upson, 1993: Sampling errors in rainfall estimates by multiple satellites. *J. Appl. Meteor.*, **32**, 399-410.
- Olson, W. S., 1989: Physical retrieval of rainfall rates over the ocean by multispectral radiometry: Application to tropical cyclones. *J. Geophys. Res.*, **94**, 2267-2280.
- Roberti, L., J. Haferman and C. Kummerow, 1994: Microwave Radiative Transfer Through Horizontally Inhomogeneous Precipitating Clouds. *J. Geophys. Res.*, **99**, 16707-16718.
- Rodgers, E. B., H. Siddalingaiah, A. T. C. Chang, and T. T. Wilheit, 1979: A statistical technique for determining rainfall over land employing Nimbus 6 ESMR measurements. *J. Appl. Meteorol.*, **18**, 978-991.
- Smith, E. A., X. Xiang, A. Mugnai, and G. Tripoli, 1994: Design of an inversion-based precipitation profile retrieval algorithm using an explicit cloud model for initial guess microphysics. *Meteorol. Atmos. Phys.*, **54**.
- Tao, W. -K., J. Simpson, S. Lang, M. McCumber, R. Adler and R. Penc, 1990: An algorithm to estimate the heating budget from vertical hydrometeor profiles. *J. Appl. Meteorol.*, **29**, 1232-1244.

- Tao, W. -K., and J. Simpson, 1993: Goddard Cumulus Ensemble model, Part I: Model description. *TAO*, **4**, 35-72.
- Tao, W. -K., S. Lang, J. Simpson and R. Adler, 1993: Retrieval algorithms for estimating the vertical profiles of latent heat release: Their applications for TRMM. *J. Meteorol. Soc. Japan*, **71**, 685-700.
- Tesmer, J. R., 1995: An improved microwave radiative transfer model for tropical oceans; Ph.D. Thesis, Department of Meteorology, Texas A&M University.
- Tripoli, G. J., 1992: An explicit three-dimensional nonhydrostatic numerical simulation of a tropical cyclone. *Meteorol. Atmos. Phys.*, **49**, 229-254.
- Wang, S., A., 1996: Modeling the beamfilling correction for microwave retrieval of oceanic rainfall; Ph.D. Thesis, Department of Meteorology, Texas A&M University.
- Weinman, J. A., and P. J. Guetter, 1977: Determination of rainfall distributions from microwave radiation measured by the Nimbus 6 ESMR. *J. Appl. Meteorol.*, **16**, 437-442.
- Wilheit, T. T., A. T. C. Chang, M. S. V. Rao, E. B. Rodgers, and J. S. Theon, 1977: A satellite technique for quantitatively mapping rainfall rates over the ocean. *J. Appl. Meteor.*, **16**, 551-560.
- Wilheit, T. T., A.T.C. Chang and L.S. Chiu, 1991: Retrieval of monthly rainfall indices from microwave radiometric measurement using probability distribution functions. *J. Atmos. Oceanic. Technol.*, **8**, 118-136.